1-1-2013

# Halo Nuclei Interactions Using Effective Field Theory

Lakma K (Lakma Kaushalya) Fernando

# Halo nuclei interactions using effective field theory

By

Nippalage Lakma Kaushalya Fernando

A Dissertation
Submitted to the Faculty of
Mississippi State University
in Partial Fulfillment of the Requirements
for the Degree of Doctor of Philosophy
in Engineering with an Emphasis in Applied Physics
in the Department of Physics and Astronomy

Mississippi State, Mississippi

August 2013

Halo nuclei interactions using effective field theory

By

Nippalage Lakma Kaushalya Fernando

Approved:

| | |
|---|---|
| Gautam Rupak Lan Tai Moong<br>Assistant Professor<br>Physics and Astronomy<br>(Major Professor) | Dipangkar Dutta<br>Associate Professor<br>Physics and Astronomy<br>(Committee Member) |
| James A. Dunne<br>Professor<br>Physics and Astronomy<br>(Committee Member) | David L. Monts<br>Professor and Graduate Coordinator<br>Physics and Astronomy<br>(Committee Member) |
| Radhakrishnan Srinivasan<br>Assistant Research Professor<br>Agricultural and Biological Engineering<br>(Committee Member) | Royce O. Bowden<br>Interim Dean of the Bagley<br>College of Engineering |

Name: Nippalage Lakma Kaushalya Fernando

Date of Degree: August 17, 2013

Institution: Mississippi State University

Major Field: Engineering with an Emphasis in Applied Physics

Major Professor: Dr. Gautam Rupak Lan Tai Moong

Title of Study: Halo nuclei interactions using effective field theory

Pages of Study: 82

Candidate for Degree of Doctor of Philosophy

Effective field theory (EFT) provides a framework to exploit separation of scales in the physical system in order to perform systematic model-independent calculations. There has been significant interest in applying the methods of EFT to halo nuclei. Using halo effective field theory, I provide a model-independent calculation of the radiative neutron capture on lithium-7 over an energy range where the contribution from the $3^+$ resonance becomes important. This reaction initiate the sequence in the carbon-nitrogen-oxygen (CNO) cycle in the inhomogeneous BBN models, and determine the amount of heavy element production from its reaction rate. One finds that a satisfactory description of the capture reaction, in the present single-particle approximation, suggests the use of a resonance width about three times larger than the experimental value. Power counting arguments that establish a hierarchy for the electromagnetic one- and two-body currents is also presented. The neutron capture of Lithium7 calculation has direct impact on the proton capture on beryllium-

7 which plays an important role in the neutrino experiments studying physics beyond the Standard Model of particle physics.

As a further study of halo nuclei interactions, the cross section of radiative capture of a neutron by carbon-14 is calculated by considering the dominant contribution from electric dipole transition. This is also a part of the CNO cycle and as the slowest reaction in the chain it limits the flow of the production of heavier nuclei $A > 14$. The cross section is expressed in terms of the elastic scattering parameters of an effective range expansion. Contributions from both the resonant and non-resonant interactions are calculated. Significant interferences between these leads to a capture contribution that deviates from a simple Breit-Wigner resonance form.

Using EFT, I present electromagnetic form factors of several halo nuclei. The magnetic dipole moment and the charge radii of carbon-15, beryllium-11, and carbon-19 halo systems are considered. Prediction is made for the magnetic moment in the leading order. I can only provide some estimates for the form factors in next-to-leading order where two-body currents appear. The estimates are based on power counting unless the effective range and the magnetic moment are known. Charge radii for three systems have also been estimated at LO and NLO.

Key words: radiative capture, halo nuclei, effective field theory, electromagnetic form factor

DEDICATION

To My Parents

ACKNOWLEDGEMENTS

The work presented in this dissertation would have been impossible without the continuous help and guidance of Dr. Gautam Rupak, my dissertation advisor, who has supported me throughout my dissertation with his knowledge and patience. He constantly encouraged and motivated me to perform my research studies independently under his supervision.

I would like to thank several other people who supported me over the years to make my dream a success. Firstly, I would like to thank all the faculty and staff at the University of Kelaniya, Sri lanka for their teaching, support, guidance, and inspiration about physics. They lead me on a strong platform to discover more in the area of nuclear physics. Moreover, I would like express my gratitude to Dr. Mark Novotny and the graduate committee for accepting me to the graduate program at Mississippi State University and supporting my studies by providing a teaching assistantship. Special thank goes to Dr. David Monts for his prompt responses and guidance provided over the past five years.

Further, I would like to thank Dr. Renato Higa, professor form university of Sao Paulo Brazil, and my group member Akshay Vaghani for their successful collaborative work. I thank my committee members: Dr. James Dunne, Dr. Dipangkar Dutta, Dr. David Monts, and Dr. Radhakrishnan Srinivasan for their comments and suggestions.

I would like to express my appreciation of the support given by all the other faculty and staff at the Department of Physics and Astronomy at Mississippi State University over

the past five years. Furthermore, I would like to thank the Bagley College of Engineering at Mississippi State University for providing me a Bagley fellowship in 2012-2013 with a travel grant.

This journey would not have been possible without the love and support of my loving parents Turin Fernando and Vinitha Perera . I also thank my husband Christopher Vanlangenberg for his understanding, patience and love during the past few years. Relocating to the USA and living in Starkville would have been difficult without the friendship and support of Laalitha Liyange, Kaumal Migelhewa, and Jehan Seneviratne, and all of my Starkville friends. I have wonderful memories which will be in my heart always.

This work was partially supported by HPC$^2$ Center for Computational Sciences at Mississippi State University through U.S. NSF Grant No. PHY-0969378.

TABLE OF CONTENTS

LIST OF TABLES

LIST OF FIGURES

LIST OF SYMBOLS, ABBREVIATIONS, AND NOMENCLATURE

**BBN:** Big-bang nucleosynthesis.

**QCD:** Quantum chromodynamics.

**EFT:** Effective field theory.

**ERE:** Effective range expansion.

**EFT:** Effective field theory.

**LO:** Leading order.

**NLO:** Next-to-leading order.

**N$^2$LO:** Next-to-next-to leading order.

**E1:** Electric dipole

**M1:** Magnetic dipole

# CHAPTER 1

# INTRODUCTION

Central goal in nuclear physics is to understand nuclear structure and reactions from the first principle. Protons and neutrons, collectively called nucleons, that make up the atomic nuclei are known to interact with each other via strong nuclear force. Quantum chromodynamics (QCD) is the fundamental theory of the strong nuclear force which describes interactions between the quarks through the exchange of gluons [1]. QCD predictions have been tested experimentally at higher energy with great precision. In the low-energy regime, relevant for nuclear structure and reactions, the nuclear interaction becomes strong. This energy is insufficient to probe detail sub structure of the hadrons. Then the low-energy degrees of freedom are no longer quarks and gluons, but rather hadrons. At these energies, effective field theory (EFT) provides a rigorous model-independent formalism for calculating nuclear properties from QCD principles, directly working with protons, neutrons and pions.

EFT provides a natural scheme for separating high-momentum (short-distance) physics $\Lambda$ from the low momentum (long-distance) $Q$ effects. As an example, for deuteron, the binding momentum, $\gamma \sim 45$ MeV, mass of pion $m_\pi \sim 140$ MeV, and mass of a nucleon $M_N \sim 1000$ MeV satisfy the momentum hierarchy $\gamma \ll m_\pi \ll M_N$. At a given external momentum $p \sim m_\pi$ we can set $m_\pi, p \sim Q$, and $M_N \sim \Lambda$. Calculations in EFT are

organized as an expansion of $Q/\Lambda$, at any given order in the expansion one includes all the quantum operators in the EFT allowed by the QCD low-energy symmetries. This ensure that the EFT are model independent at every order in the expansion. Accuracy of the EFT calculations can be systematically improved as long as there is a clear separation between the energy scales, $Q \ll \Lambda$. The uncertainty associated with a calculation of any observable in an EFT can be estimated from the $Q/\Lambda$ expansion. The set of rules which guides the construction of this expansion is called the power counting. One can *a priori* estimate the size of the coupling and interactions based on power counting. If the power counting is consistent, then the EFT calculation should produce data as well as contributions from different orders in the perturbation that have sizes compatible to the prior estimates. If it is consistent, then it is an indication that the power counting is valid and EFT error estimates are reliable.

Briefly the basics strategies in an EFT calculation are: (i) identify the low-energy degree of freedom based on the low-energy scales and symmetries, (ii) construct a power counting from the relevant energy scales, (iii) write down the interaction based on the low-energy symmetries, (iv) use the power counting rules to limit the number of interactions in the given order, and (v) determine the unknown couplings from data and check whether the power counting assumptions hold.

There are several phenomenological models that are available to study multi-nucleon systems. Potential model calculations describe two nucleon (NN) data and deuteron properties precisely [2, 3, 4], and can reproduce the properties of light nuclei. In these models, the short-range nuclear force treatments differ considerably. From the EFT perspective,

these differences correspond to different choices of coupling associated with some of the multi-nucleon operators. As an example, a two-body axial current operator in EFT explains differences in the calculation of inelastic neutrino-deuteron scattering cross sections from different potential models [5]. There is no inherent methods of estimating errors in potential model calculations. Typically, one compares the results from potential model calculations to estimate the theoretical error; however, in EFT calculations one can make self consistent error estimate based on the power connoting.

The present work concerns halo nuclei. Halo nuclei are weakly-bound clusters rather than a tight shell-like structure. The last one or two valence nucleons (usually neutrons) are decoupled from a well-defined inert core that contain all the other nucleons. The separation energy of the valence nucleons is much lower than the energy needed to break up the core. The fields of nuclear structure and reactions have witnessed continuous progress and renewal of interest with the advent of present and future facilities that are able to provide high-intensity beams of very unstable, rare isotopes so called exotic nuclei, whose physical properties are in the process of being uncovered. A subset in this exotic zoo comprises halo nuclei with a slowly decreasing wave function tail that extends much farther than the effective core-nucleon interaction. Such an extended and dilute configuration leads to threshold phenomena with consequences for low-energy nuclear astrophysics [6, 7]. While $^{6}$He, $^{11}$Li, and $^{11}$Be are the most studied halo nuclei; $^{14}$Be, $^{14}$B, $^{8}$Li, $^{15}$C and $^{19}$C are also confirmed as halo. All the above are examples of neutron halo systems, and all lie on or are close to the neutron dripline at the limits of neutron stability. Since higher angular momentum values give rise to a confining centrifugal barrier, the valence nucleons must be

in a relatively low orbital angular momentum state, preferably a $s$-wave. Proton halos are expected to be less abundant because of the Coulomb barrier. Nevertheless, there are few proton halos including, $^{8}$B, $^{13}$N,$^{17}$Ne, and the first excited state of $^{17}$Fe [8].

The field of halo nuclei has generated much excitement since its discovery in the mid-1980s. Tanihata and his group discovered much larger cross section values for $^{11}$Li and $^{6}$He than was expected [9, 10]. Unexpected cross section results lead to larger values of rms radii than the $\mathrm{A}^{\frac{1}{3}}$ perdictions from liquid drp models. Later, the reason for this unexpected behavior was recognized as the halo effect [11]. Abundance of heavy elements in nature cannot be explained without considering halo nuclear reactions in the big bang nucleosynthesis (BBN) or stellar burning as the heavier element production mechanism proceeds through those exotic nuclei. As an example, halo nuclear reaction $^{14}\mathrm{C}(n,\gamma)^{15}\mathrm{C}$ is a part of the CNO cycle which is one of the main energy sources in the helium burning layer of asymptotic giant branch stars and in the core helium burning of massive stars [12]. Experiments on halos are carried out at ATLAS at Argonne and NSCL at Michigan State University. Future experiments are planned at the Facility of Rare Isotope Beams (FRIB). There is renewed interest in the study of halo nuclei due to the advent of present and planned experiments with high intensity beams of exotic radioactive rare isotopes.

There are several other theoretical approaches to study halo nuclei, such as *ab initio* calculations [13, 14], few body methods for the core and valence nucleons [15], and semi-classical methods such as Glauber model [16] that are also available to study these interactions. The EFT for few nucleon systems with large scarring length, have been very successful recently, can also be extend to be study halo nuclei. This is due to the fact that

there is clear separation of energy between the energy need remove the valence nucleons versus the energy need to break up the core.

Here my goal is to study several halo nuclei interactions using EFT. The EFT calculations of halo properties was initiated in Ref.[17, 18], and those studies demonstrated that the EFT is an ideal tool to study halo nuclei with reliable error estimates. It has been used to study $s$-wave alpha-alpha resonance [19, 20], three-body halo nuclei [21, 22], electromagnetic transitions and transition probability strength in one-neutron halo $^{11}$Be [23, 24], and proton-$^7$Li interaction in coupled-channel extension [25]. Binding momentums of these halo nuclei are of the order of $Q$ and $\ll m_\pi$(pion mass); as a result, pions can be integrated out from the theory. EFT calculations are important because they not only provide cross section calculations but also reliable error estimates. This is important because many of the astrophysical reactions occur at energies that make experimental measurements difficult. A low-energy nuclear EFT is formulated not only to study halo nuclei bound states but also interactions.

While $^7\mathrm{Li}(n,\gamma)^8\mathrm{Li}$ has its own astrophysical interests, such as initiating the sequence in the carbon-oxygen-nitrogen (CNO) in inhomogeneous BBN models, and determining the amount of heavy elements production from its reaction rate [26], it is an iso-spin mirror system of $^7\mathrm{Be}(p,\gamma)^8\mathrm{B}$ which is important as the main source of boron-8 solar neutrinos that are been detected in neutrino experiments. Direct measurements of $^7\mathrm{Be}(p,\gamma)^8\mathrm{B}$ at the relevant solar energy, $20$ keV, is difficult due to the Coulomb barrier. Currently, experiments are done above $\sim$ $100$ keV has to be extrapolated down to the solar energy. Theoretical calculations are necessary for this extrapolation which are estimated to have

an error of $5-20\%$ [27, 28, 29]. EFT play an important role here in accurately estimating the errors in the extrapolation.

Traditionally, theoretical calculations are tested in iso-spin mirror system by calculating the $^7\mathrm{Li}(n,\gamma)^8\mathrm{Li}$. Here one can study the nuclear short-range interactions without worrying about the Coulomb force. As both the $^7\mathrm{Be}(p,\gamma)^8\mathrm{B}$ and $^7\mathrm{Li}(n,\gamma)^8\mathrm{Li}$ involve the same spin channel, the structure of the nuclear interactions in the $^7\mathrm{Be}(p,\gamma)^8\mathrm{B}$ can be calculated directly from the $^7\mathrm{Li}(n,\gamma)^8\mathrm{Li}$ calculations. Here my work involve the calculation of $^7\mathrm{Li}(n,\gamma)^8\mathrm{Li}$ using EFT. There is elastic scattering data for $n+Li$ system that allows us to determine the unknown EFT couplings in the channels. Future studies would involve the calculation of $^7\mathrm{Be}(p,\gamma)^8\mathrm{B}$ by adding the Coulomb contribution to the EFT results from $^7\mathrm{Li}(n,\gamma)^8\mathrm{Li}$ [28].

$^{14}\mathrm{C}(n,\gamma)^{15}\mathrm{C}$ is also a part of the CNO cycle and plays an important role in astrophysics, the slowest reaction in the cycle which leads to a substantial enrichment in $^{14}$C abundance.

Later in the dissertation, I describe how to apply EFT to find electromagnetic form factors of halo nuclei ground states of $\frac{1}{2}^+$ by considering $^{11}$Be, $^{15}$C and $^{19}$C nuclei. Depending on the available experimental data the magnetic moment and charge radii of the three systems are predicted or estimated.

Experimentally, the binding energies of $^{15}$C and $^8$Li are found to be $1.218$ MeV and $2.032$ MeV, respectively; consequently, the ground states of both $^{15}$C and $^8$Li are considered as shallow bound states because the binding energy is much below the high-energy scale $\Lambda$, in our case it is $m_\pi$, and then the low-energy degrees of freedom are only the nu-

cleons. As the binding energy is very small compared to the energy needed to break up the core, $^8$Li and $^{15}$C can be treated as a core plus a valence neutron. The ground state of $^8$Li is a $p$-wave, and it is $s$-wave for $^{15}$C. Possible transitions between the initial and the final states are identified from parity conservation. The study of $^7\mathrm{Li}(n,\gamma)^8\mathrm{Li}$, an extension of the previous work of Gautam Rupak and Renato Higa, includes the complete E1 transition at leading order, as well as the leading M1 capture at low energies. $^{14}\mathrm{C}(n,\gamma)^{15}\mathrm{C}$ is calculated by considering the contribution from an E1 transition between the initial $p$-wave to final $s$-wave ground state of $^{15}$C, and M1 transition is suppressed (at one-body current level) due to the orthogonality of the continuum and bound state wave functions.

The work presented here is a collaboration with Gautam Rupak, Renato Higa, and Akshay Vaghani. The organization of the dissertation is as follows: In Chapter 2, the leading E1 and M1 contributions of the radiative neutron capture of Lithium-7 is calculated over an energy range where the contribution from the $3^+$ resonance becomes important. Halo EFT is used to study the other reaction, $^{14}\mathrm{C}(n,\gamma)^{15}\mathrm{C}$, by considering both resonant and non-resonant interaction, in Chapter 3. Chapter 4 deals with the electromagnetic form factors for several halo systems that I mentioned above. Conclusions and future directions are presented in Chapter 5.

# CHAPTER 2

# RADIATIVE NEUTRON CAPTURE ON LITHIUM-7

Low energy nuclear reactions play an important role in understanding element formation, testing astrophysical models and physics beyond the standard model of particle physics. Often terrestrial laboratories do not have direct access to the energies at which these key reactions occur. An example for such a reaction is the radiative proton capture of beryllium-7 $^7\mathrm{Be}(p,\gamma)^8\mathrm{B}$, which is important for boron-8 production in the sun. Underground neutrino detectors at SNO and Super-K are sensitive to neutrinos coming from $\beta$-decay of $^8$B. While the known experimental data remain above 100 keV, the relevant solar energy for this reaction is around 20 keV, the Gamow peak [27]. A theory is necessary to extrapolate known data to the low energies as the measurements at low energies are difficult, mainly due to Coulomb repulsion. Available theoretical approaches [30, 31, 32, 33, 34, 35, 36, 37, 29, 38, 28, 39] that use the $p$-$^7\mathrm{Be}$ data alone, even with scattering information, are not well-constraining. Current extrapolations introduce 5% -20% error [27, 28, 29]. A model independent effective field theory calculation would be very useful in constraining them.

Boron-8, an example of a proton halo, is a nucleus with a proton weakly bound to beryllium-7 by 0.1375 MeV. The calculation of the $^7\mathrm{Be}(p,\gamma)^8\mathrm{B}$ reaction would be an important step in developing EFT techniques for weakly bound systems. Future planned

experiments at the Facility for Rare Isotope Beams (FRIB) would explore exotic nuclei, including halos near the drip lines [40]. Halo EFT calculations on structure and reactions can serve as a benchmark for phenomenological models.

The low energy reaction $^7\mathrm{Li}(n,\gamma)^8\mathrm{Li}$ which is an isoispin mirror to the $^7\mathrm{Be}(p,\gamma)^8\mathrm{B}$ is considered. Lithium-8 is a neutron halo which can be described as a neutron weakly bound to lithium-7. At low energy a single-particle description of $^8\mathrm{Li}$ as a $^7\mathrm{Li}$ core plus a valence neutron is appropriate [28, 38, 39]. This system allows to formulate the EFT calculation for the interactions without the complication of the Coulomb force, and more precise data at very low energies are also available. The mirror system $n$-$^7\mathrm{Li}$ then becomes an important ingredient for benchmarking purposes. Besides guiding the $^7\mathrm{Be}(p,\gamma)^8\mathrm{B}$ calculation, $n$-$^7\mathrm{Li}$ has astrophysical interest. It is a key process in inhomogeneous BBN models. $^7\mathrm{Li}$ initiates the sequence in the CNO cycle, and its reaction rate is crucial in determining the amount of heavy element production [26].

The $^7\mathrm{Li}(n,\gamma)^8\mathrm{Li}$ cross section was calculated recently by effective field theory (EFT) for halo nuclei at low energy [41]. In this framework, the tight $^7\mathrm{Li}$ core, inert and structureless at leading order (LO), the loosely bound neutron, and the external soft photons are the relevant degrees of freedom. The main assumption of the approach is a single-particle approximation, somewhat similar to models like Refs. [38, 42, 28, 39], where the valence nucleon interacts with the core via a Woods-Saxon potential. In halo EFT, however, a systematic and model-independent expansion of observables is achieved through the use of an expansion parameter formed by the ratio of a soft scale $Q$, associated with the shallowness of the valence neutron, and a hard scale $\Lambda$, related to the tightness of the core.

This chapter is organized as follows: In Section. 2.1 I develop the basic theory for the interactions necessary to calculate the capture reaction $^7\mathrm{Li}(n,\gamma)^8\mathrm{Li}$. Further, I present the Lagrangian for elastic scattering in the $s$- and $p$-waves in the $n+^7\mathrm{Li}$ system and derive the one-body (magnetic moment) and two-body currents. Then I describe how the couplings in the EFT Lagrangian are constrained from the available data on low-lying bound and resonance states. Results are shown in Section. 2.2 and compared with some available data and potential model calculations. I also present a brief discussion on higher-order terms and other degrees of freedom that becomes important at energies slightly above the ones considered here.

## 2.1 Formalism

The low-energy theory for $^7\mathrm{Li}(n,\gamma)^8\mathrm{Li}$ is constructed from the spin parity state $\frac{1}{2}^+$ for the neutron and $\frac{3}{2}^-$ state for lithium-7 while the final $^8\mathrm{Li}$ nucleus contains $2^+$ and $1^+$ ground and excited states. At energies around 200 keV, a $p$-wave resonance is noticeable and that state is identified as a $3^+$ state. When developing the theory, it is useful to list all the possible initial and final channels for the reaction. From the spectroscopic notation $^{2S+1}L_J$, concentrating only on the $s$- and $p$-waves, the initial $s$-wave states are $^3S_1$ and $^5S_2$, the final $p$-wave states are $^3P_2$, $^5P_2$ for the ground state and $^3P_1$, $^5P_1$ channels are for the excited state, and the initial $p$-wave resonant state is $^5P_3$.

Quantum numbers of both $^3P_2$ and $^5P_2$ states represent the $2^+$ ground state of lithium-8; however, from the symmetric condition, it is identified as $|2^+\rangle \equiv (|^3P_2\rangle + |^5P_2\rangle)/\sqrt{2}$ [43]. Further, the $1^+$ excited state is primarily dominated by the antisymmetric combination

$|1^+\rangle \equiv (|^5P_1\rangle - |^3P_1\rangle)/\sqrt{2}$ [35]. In the present $n +^7$ Li approach, the $3^+$resonance can only belong to the $^5P_3$ channel.

Transition from the initial $^3S_1$ and $^5S_2$ states to the $2^+$ ground state is the leading contribution to the capture cross section which proceeds through an E1 transition due to the electromagnetic selection rules (parity conservation), and a small contribution from the E1 capture to the excited $1^+$ state with a branching ratio of $0.106$ [44]. Finally, the M1 contribution from the $3^+$ resonance to the $2^+$ ground state occurs at en energy around 200 keV.

In Ref. [41], the authors used the Clebsch-Gordan coefficient matrices

$$\begin{aligned} S_1 &= \frac{1}{\sqrt{6}} \begin{pmatrix} -\sqrt{3} & 0 & 1 & 0 \\ 0 & -1 & 0 & \sqrt{3} \end{pmatrix} \\ S_2 &= -\frac{i}{\sqrt{6}} \begin{pmatrix} \sqrt{3} & 0 & 1 & 0 \\ 0 & 1 & 0 & \sqrt{3} \end{pmatrix} \\ S_3 &= \frac{2}{\sqrt{6}} \begin{pmatrix} 0 & 1 & 0 & 0 \\ 0 & 0 & 1 & 0 \end{pmatrix} \end{aligned} \tag{2.1}$$

which satisfy

$$S_i S_j^\dagger = \frac{2}{3}\delta_{ij} - \frac{i}{3}\epsilon_{ijk}\sigma_k\,, \qquad S_i^\dagger S_j = \frac{3}{4}\delta_{ij} - \frac{1}{6}\big\{J_i^{(3/2)}, J_j^{(3/2)}\big\} + \frac{i}{3}\epsilon_{ijk}J_k^{(3/2)}\,, \tag{2.2}$$

where $J_i^{(3/2)}$'s are the generators of spin-3/2. We construct the following Clebsch-Gordan coefficient matrices

$$F_i = -\frac{i\sqrt{3}}{2}\sigma_2 S_i, \qquad\qquad Q_{ij} = -\frac{i}{\sqrt{8}}\sigma_2\big(\sigma_i S_i + \sigma_j S_i\big), \tag{2.3}$$

to project the neutron $N(x)$ and lithium-7 $C(x)$ fields onto the spin $S = 1$ and spin $S = 2$ channels as $N^T F_i C$ and $N^T Q_{ij} C$, respectively. The vector index $F_i$ is related to the three magnetic quantum numbers in spin $S = 1$ and $Q_{ij}$, symmetric traceless matrices, are related to the five quantum numbers in spin $S = 2$. The same formalism use here to construct all the relevant initial and final states.

### 2.1.1 Interaction Lagrangian and magnetic moment coupling

#### 2.1.1.1 Initial state elastic scattering in $s$-wave

According to Ref [41], the $s$-wave interaction Lagrangian is written as

$$\mathcal{L}_s = g^{(1)}(N^T F_i C)^\dagger (N^T F_i C) + g^{(2)}(N^T Q_{ij} C)^\dagger (N^T Q_{ij} C) + \cdots , \tag{2.4}$$

where the "$\cdots$" represents higher derivative terms that are suppressed at low energy. At LO, there is a single coupling $g^{(s)}$ in the ${}^5S_2$ (${}^3S_1$) spin channel that is fixed from the known $s$-wave scattering length $a_0^{(2)} = -3.63 \pm 0.05$ fm ($a_0^{(1)} = 0.87 \pm 0.07$ fm) [45, 46].

#### 2.1.1.2 Elastic scattering in $p$-wave

The description of a low-energy $p$-wave bound/excited state or resonance requires two operators at LO [17, 18]. For our convenience we work in the dimer formalism where the four-fermion contact interaction is replaced by the exchange of an auxiliary dimer field $\phi(x)$. The $p$-wave interaction Lagrangian then reads

$$\mathcal{L}_p^{(\eta)} = \phi_{[j]}^{(\eta)\dagger} \left[ \left( i\partial_0 + \frac{\nabla^2}{2M} \right) + \Delta^{(\eta)} \right] \phi_{[j]}^{(\eta)} + h^{(\eta)} \left[ \phi_{[j]}^{(\eta)} N^T P^{(\eta)} C + \text{H. c.} \right] , \tag{2.5}$$

where $M = M_n + M_c$, neutron mass $M_n = 939.6$ MeV, ${}^7$Li mass $M_c = 6535.4$ MeV and H.c. stands for Hermitian conjugate. $P_{[j]}^{(\eta)}$ are the projectors for the relevant $p$-wave

channels: ${}^3P_1$, ${}^3P_2$, ${}^5P_1$, ${}^5P_2$, and ${}^5P_3$ indicated by the superscript index $\eta$. The subscript $[j]$ is a single, double, or triple tensor index as appropriate for $J = 1$, $J = 2$ and $J = 3$ states, respectively. All these elements, together with the matrices $F_i$ and $Q_{ij}$ from Eq. (2.3), allow us to build the operators, in coordinate space,

$$
\begin{aligned}
P_i^{({}^3P_1)} &= \sqrt{\frac{3}{2}} F_x \left( \frac{\overrightarrow{\nabla}}{M_c} - \frac{\overleftarrow{\nabla}}{M_n} \right)_y \epsilon_{ixy}, \\
P_{ij}^{({}^3P_2)} &= \sqrt{3} F_x \left( \frac{\overrightarrow{\nabla}}{M_c} - \frac{\overleftarrow{\nabla}}{M_n} \right)_y R_{xyij}, \\
P_i^{({}^5P_1)} &= \sqrt{\frac{9}{5}} Q_{ix} \left( \frac{\overrightarrow{\nabla}}{M_c} - \frac{\overleftarrow{\nabla}}{M_n} \right)_x, \\
P_{ij}^{({}^5P_2)} &= \frac{1}{\sqrt{2}} Q_{xy} \left( \frac{\overrightarrow{\nabla}}{M_c} - \frac{\overleftarrow{\nabla}}{M_n} \right)_z T_{xyzij}, \\
P_{ijk}^{({}^5P_3)} &= \sqrt{3} Q_{xy} \left( \frac{\overrightarrow{\nabla}}{M_c} - \frac{\overleftarrow{\nabla}}{M_n} \right)_z G_{ijkxyz},
\end{aligned}
\tag{2.6}
$$

with the tensors

$$
\begin{aligned}
R_{ijxy} &= \frac{1}{2} \left( \delta_{ix}\delta_{jy} + \delta_{iy}\delta_{jx} - \frac{2}{3}\delta_{ij}\delta_{xy} \right), \\
T_{xyzij} &= \frac{1}{2} \Big( \epsilon_{xzi}\delta_{yj} + \epsilon_{xzj}\delta_{yi} + \epsilon_{yzi}\delta_{xj} + \epsilon_{yzj}\delta_{xi} \Big), \\
G_{ijklmq} &= \frac{1}{6} \Bigg\{ - \frac{2}{5} \Big[ \delta_{qm}(\delta_{il}\delta_{jk} + \delta_{jl}\delta_{ik} + \delta_{ij}\delta_{kl}) + \delta_{ql}(\delta_{im}\delta_{jk} + \delta_{jm}\delta_{ik} + \delta_{ij}\delta_{km}) \\
&\quad + \delta_{lm}(\delta_{iq}\delta_{jk} + \delta_{jq}\delta_{ik} + \delta_{ij}\delta_{kq}) \Big] + (\delta_{il}\delta_{jm}\delta_{kq} + \delta_{il}\delta_{jq}\delta_{km}) \\
&\quad (\delta_{jl}\delta_{km}\delta_{iq} + \delta_{jl}\delta_{kq}\delta_{im}) + (\delta_{kl}\delta_{im}\delta_{jq} + \delta_{kl}\delta_{iq}\delta_{jm}) \Bigg\}.
\end{aligned}
\tag{2.7}
$$

They have properties

$$
\begin{aligned}
R_{ijlm} &= R_{jilm} = R_{ijml} = R_{lmij}\,, \\
T_{ijklm} &= T_{jiklm} = T_{ijkml} = -T_{lmkij}\,, \\
G_{ijklmq} &= G_{jiklmq} = G_{kjilmq} = G_{ikjlmq} = G_{ijkmlq} = G_{ijkqml} = G_{ijklqm} = G_{lmqijk}\,, \\
&\Rightarrow \quad R_{ijxy}R_{xylm} = R_{ijlm}\,, \qquad R_{ijxy}T_{xyklm} = T_{ijkxy}R_{xylm} = T_{ijklm}\,, \\
&\qquad G_{abcijk}G_{ijklmn} = G_{abclmn} = R_{abxy}G_{xyclmn}\,. \qquad (2.8)
\end{aligned}
$$

It is straightforward to verifify that

$$
\mathrm{Tr}[F_i F_j^\dagger] = \delta_{ij}\,, \qquad \mathrm{Tr}[Q_{ij}Q_{lm}^\dagger] = R_{ijlm}\,. \qquad (2.9)
$$

We also introduce the photon vectors and tensors ($\varepsilon_i^{(\gamma)}$), spin-1 ($\varepsilon_j$), spin-2 ($\varepsilon_{ij}$) and spin-3 tensor ($\varepsilon_{ijk}$) polarizations, obeying the following sums [47, 48],

$$
\begin{aligned}
&\sum_{\text{pol.}} \varepsilon_i^{(\gamma)}\varepsilon_j^{(\gamma)*} = \delta_{ij} - \frac{k_i k_j}{k^2}\,, \sum_{\text{avg.pol.}} \varepsilon_i\varepsilon_j^* = \frac{\delta_{ij}}{3}\,, \sum_{\text{avg.pol..}} \varepsilon_{ij}\varepsilon_{lm}^* = \frac{R_{ijlm}}{5}\,, \qquad (2.10) \\
&\sum_{\text{avg.pol.}} \varepsilon_{ijk}\varepsilon_{lmq}^* = \frac{G_{ijklmq}}{7}\,.
\end{aligned}
$$

#### 2.1.1.3 Magnetic moment couplings

To describe the capture through the $3^+$ resonance state, the magnetic moment operators are needed

$$
O^M = g_n \mu_N N^T \left(\frac{\boldsymbol{\sigma}}{2}\cdot\boldsymbol{B}\right) N + g_c \mu_N C^T \left(\boldsymbol{J}\cdot\boldsymbol{B}\right) C, \qquad (2.11)
$$

where $\boldsymbol{\sigma}$ are the Pauli matrices, $\boldsymbol{J}$ are the angular momentum matrices for spin-3/2 particle, $\boldsymbol{B} = \boldsymbol{\nabla}\times\boldsymbol{A}$ is the magnetic field, $\mu_N$ is the nuclear magneton, and $g_n \equiv 2\kappa_n$ and

$g_c = 2\kappa_c/3$ are the neutron and the $^7$Li gyromagnetic ratios, respectively. We take $\kappa_n = -1.91304$ and $\kappa_c = 3.256427$ as the corresponding magnetic moments [49].

#### 2.1.1.4 Two-body current

Two-body current is allowed by symmetry and contribute to the magnetic dipole transition from the initial $^5P_3$ state to the final $^5P_2$ and $^3P_2$ states. It can be written as

$$O^L = i\mu_N\, L^{(2)} {\phi_{ij}^{(^5P_2)}}^\dagger B_k \phi_{lmq}^{(^5P_3)} G_{ijklmq} + \mu_N\, L^{(1)} {\phi_{ij}^{(^3P_2)}}^\dagger B_k \phi_{lmq}^{(^5P_3)} G_{ijklmq} + \text{H.c.}. \quad (2.12)$$

Two-body couplings $L^{(1)}$ and $L^{(2)}$ also regulate the divergences that appear in certain loop diagrams.

### 2.1.2 Determining the EFT couplings

#### 2.1.2.1 Elastic scattering parameters of $s$-wave and $p$-wave

The unknown couplings $g^{(s)}$ and $h^{(\eta)}$ in Eqs. (2.4) and (2.5) can be related to the elastic scattering data in the $s$- and $p$-waves when available. Therefore, it is appropriate to match field theory to the low-energy amplitude written in terms of the effective range expansion (ERE).

The ERE elastic scattering amplitude in the $\ell$-th partial wave is written as

$$i\mathcal{A}_\ell(p) = \frac{2\pi}{\mu}\frac{ip^{2\ell}}{p^{2\ell+1}\cot\delta_\ell - ip^{2\ell+1}} = \frac{2\pi}{\mu}\frac{ip^{2\ell}}{-1/a_\ell + \frac{1}{2}r_\ell p^2 + \frac{1}{2}t_\ell p^4 + \cdots - ip^{2\ell+1}}, \quad (2.13)$$

using

$$p^{2\ell+1}\cot\delta_\ell = \frac{1}{a_\ell} + \frac{1}{2}r_\ell p^2 + \frac{1}{2}t_\ell p^4 + \cdots, \quad (2.14)$$

with reduced mass $\mu = \frac{M_C M_N}{M_C + M_N}$, and $a_\ell$, $r_\ell$, $t_\ell$, etc., are ERE parameters. Each term is assigned a momentum scaling which, in general, is given by dimensional analysis. Since the ERE parameters are associated with short-range (high-momentum $\Lambda$) nuclear interaction, naively one would expect $1/a_\ell \sim \Lambda^{2\ell+1}$, $r_\ell \sim \Lambda^{2\ell-1}$, $t_\ell \sim \Lambda^{2\ell-3}$, and so on. At arbitrarily low momentum $p \sim Q$, one can expand the amplitude $\mathcal{A}_\ell$ in a Taylor series around $Q/\Lambda = 0$, a situation where the interaction is weak and perturbative. The perturbative series needs to be rearranged in order to apply this formalism for shallow bound or virtual states; however, it is only possible if at least one of the ERE parameters (usually the scattering length) has a different scaling than the one assumed by naive dimensional analysis. The $s$- and $p$-wave scattering amplitudes at LO then read [50, 51, 52, 53, 54, 55, 17, 18]

$$i\mathcal{A}_0(p) = \frac{2\pi}{\mu} \frac{i}{-1/a_0 - ip} \,, \tag{2.15}$$

$$i\mathcal{A}_1(p) = \frac{2\pi}{\mu} \frac{ip^2}{-1/a_1 + \frac{1}{2} r_1 p^2 - ip^3} \,. \tag{2.16}$$

For a shallow bound or virtual state in $s$-wave, we set $1/a_0 \sim Q$; then only one single operator is needed at LO. For a shallow $p$-wave, the situation is more subtle. First, only one particular fine-tuning of the scattering "length", $1/a_1 \sim Q^2\Lambda$, is enough to produce the shallow state [18]. However, not only one, but two operators emerge at LO, since the effective "range" term $r_1 p^2/2 \sim Q^2\Lambda$ now scales as $1/a_1$ at momenta $p \sim Q$. Second, the unitarity term $ip^3 \sim Q^3$ is in principle of higher order. The $p$-wave amplitude $\mathcal{A}_1$ is then suppressed by $Q/\Lambda$ relative to $\mathcal{A}_0$. However, for energies close to the resonant state, there is a cancellation of the leading terms (kinematical fine-tuning [18, 56]) that

makes $-1/a_1 + rp^2/2 \sim Q^3$ and promotes the unitarity term $ip^3$ to LO. In that region, the amplitudes (2.15) and (2.16) contribute at the same order.

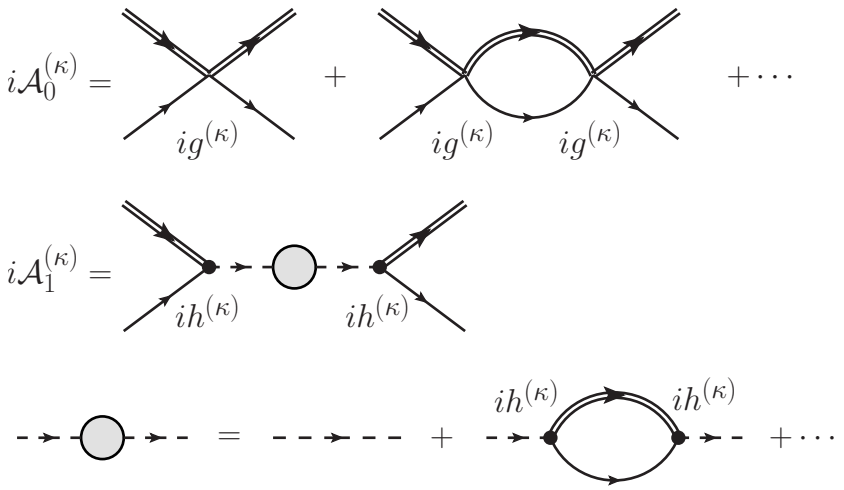


Figure 2.1

Initial $s$-wave $\mathcal{A}_0^{(\kappa)}$ and $p$-wave $\mathcal{A}_1^{(\kappa)}$ elastic scattering amplitudes

Double line is the $^7$Li propagator, single line the neutron propagator, dashed line the bare dimer propagator.

As shown in Fig. 2.1, the interactions in Eqs. (2.4) and (2.5) produce an elastic scattering amplitude in EFT and it becomes a geometric series that sums to give

$$i\mathcal{A}_0^{(\eta)}(p) = \frac{ig^{(\eta)}}{1 - ig^{(\eta)} f_0(p)}, \tag{2.17}$$
$$f_0(p) = -i2\mu \left(\frac{\lambda}{2}\right)^{4-D} \int \frac{d^{D-1}\boldsymbol{q}}{(2\pi)^{D-1}} \frac{1}{q^2 - p^2 - i0^+} = -\frac{i\mu}{2\pi}(\lambda + ip),$$

with renormalization scale $\lambda$ . Comparing Eqs. (2.17) and (2.15), we find [30-35]

$$g^{(\eta)}(\lambda) = \frac{2\pi}{\mu} \frac{1}{\lambda - 1/a_0^{(\eta)}}, \tag{2.18}$$

where $\eta = 1, 2$ correspond to spin channels $^3S_1$, $^5S_2$, respectively.

Similarly, for the $p$-wave amplitude, we have from Fig. 2.1

$$i\mathcal{A}_1^{(\eta)} = -[h^{(\eta)}]^2 \frac{p^2}{\mu^2} iD^{(\eta)}(p^2/2\mu, 0) = \frac{2\pi}{\mu} \frac{ip^2}{-\frac{2\pi\mu\Delta^{(\eta)}}{[h^{(\eta)}]^2} - \frac{\pi\lambda^3}{2} - \left(\frac{3\lambda}{2} + \frac{\pi}{[h^{(\eta)}]^2}\right) p^2 - ip^3}, \tag{2.19}$$

using the full dimer propagator

$$\begin{aligned} iD^{(\kappa)}(p_0, \boldsymbol{p}) =& \frac{i}{\Delta^{(\kappa)} - \frac{1}{2\mu}\zeta^2 + \frac{2h^{(\kappa)\,2}}{\mu} f_1(p_0, \boldsymbol{p})}, \\ f_1(p_0, \boldsymbol{p}) =& \frac{1}{4\pi}\left(\zeta^3 - \frac{3}{2}\zeta^2\lambda + \frac{\pi}{2}\lambda^3\right), \end{aligned} \tag{2.20}$$

where $\zeta = \sqrt{-2\mu p_0 + \mu p^2/M - i0^+}$. From the EFT amplitude and the $p$-wave ERE expansion, the coupling pair ($\Delta^{(\kappa)}$, $h^{(\kappa)}$) is determined. As the $s$-wave, comparing Eqs. (2.19) and (2.16) yields

$$\begin{aligned} -\frac{2\pi\mu\Delta^{(\eta)}}{[h^{(\eta)}]^2} - \frac{\pi}{2}\lambda^3 =& -1/a_1^{(\eta)}, \\ -\frac{3}{2}\lambda - \frac{\pi}{[h^{(\eta)}]^2} =& \frac{1}{2} r_1^{(\eta)}. \end{aligned} \tag{2.21}$$

The index $\eta$ identifies the relevant $p$-wave channels outlined earlier. The EFT couplings $\Delta^{(\eta)}$and $h^{(\eta)}$ are therefore fixed in terms of the ERE parameters $a_1^{(\eta)}$and$r_1^{(\eta)}$ and the renormalization scale $\lambda$.

For bound channels $1^+$ and $2^+$, we follow the procedure used in Ref. [41]. It is more convenient to work directly with the location of the pole in the dimer propagator at bind-

ing momentum $\gamma^{(\eta)}$ and its residue $\mathcal{Z}^{(\eta)}$. The latter is the wave function renormalization constant calculated using Eqs. (2.20) and (2.21) as

$$\begin{aligned}
[\mathcal{Z}^{(\eta)}]^{-1} =& \frac{\partial}{\partial p_0}[D^{(\eta)}(p_0, \boldsymbol{p})]^{-1}\big|_{p_0=\boldsymbol{p}^2/(2M)-B^{(\eta)}}, \\
\mathcal{Z}^{(\eta)} =& -\frac{2\pi}{[h^{(\eta)}]^2}\frac{1}{3\gamma^{(\eta)} + r_1^{(\eta)}},
\end{aligned} \tag{2.22}$$

where $B^{(\eta)} = [\gamma^{(\eta)}]^2/(2\mu)$ is the binding energy. The ${}^3P_2$ and ${}^5P_2$ channels in $2^+$ share a common binding momentum $\gamma^{(2^+)} \approx 57.8$ MeV. Moreover, the capture cross section is not independently sensitive to the effective range parameter $r_1$ in these two spin channels [41]. For this reason we use a common effective range parameter $r_1^{(2^+)}$. This coincidentally gives the observed ratio $0.82$ of spin channel $S = 2$ relative to the total E1 capture to the ground state at threshold [57]. We make a similar simplifying assumption for the $1^+$ state and use a common effective range parameter $r_1^{(1^+)}$ for both spin channels ${}^3P_1$ and ${}^5P_1$. In the final cross section, only the combinations

$$\begin{aligned}
[h^{(2^+)}]^2\mathcal{Z}^{(2^+)} &= -\frac{2\pi}{3\gamma^{(2^+)} + r_1^{(2^+)}}, \\
[h^{(1^+)}]^2\mathcal{Z}^{(1^+)} &= -\frac{2\pi}{3\gamma^{(1^+)} + r_1^{(1^+)}},
\end{aligned} \tag{2.23}$$

contribute to the $2^+$ and $1^+$ states, respectively. In Ref. [41], $r_1^{(2^+)} \approx -1.55$ fm$^{-1}$ from a fit to low energy data from Ref. [58]. $\gamma^{(1^+)} \approx 41.6$ MeV from the known $1^+$ excited state energy. We will determine $r_1^{(2^+)}$ and $r_1^{(1^+)}$ in this work from the known E1 thermal capture rates to the $2^+$ and $1^+$ states [44] respectively.

#### 2.1.2.2 Resonance parameters

The $p$-wave EFT couplings for the $3^+$ ($^5P_3$) state can be related to the ERE scattering parameters $a_1^{(3)}$ and $r_1^{(3)}$ through Eq (2.21). Since these ERE parameters are not known we first determine them from the known resonance energy and width. At very low momentum, the phase shift $\delta(p)$ in this channel vanishes due to the centrifugal barrier. Near resonance, $\delta(p)$ increases rapidly through $\pi/2$ from below. Thus, $\cot\delta(p)$ has to go through zero from above, *i.e.*, it has a negative slope. These conditions can be written as [59]

$$\begin{aligned} \cot\delta\Big|_{E=E_r} &= 0, \ \text{ and} \\ \frac{d}{dE}\cot\delta\Big|_{E=E_r} &= -c < 0, \end{aligned} \tag{2.24}$$

such that $c > 0$. Near resonance,

$$\begin{aligned} \cot\delta(E) \approx& \cot\delta(E_r) + (E-E_r)\cot'\delta(E_r) = -(E-E_r)c, \\ \mathcal{A}(p) =& \frac{2\pi}{\mu}\frac{1}{p\cot\delta - ip} \approx \frac{2\pi}{\mu p}\frac{-\Gamma_r/2}{(E-E_r)+i\Gamma_r/2}, \end{aligned} \tag{2.25}$$

and we recover the Breit-Wigner form, identifying $c \equiv 2/\Gamma_r$. The resonance position and width can be related to the ERE scattering parameters. In the center-of-mass (c.m.) frame define $p_r^2 \equiv 2\mu E_r$, then

$$\begin{aligned} p^3\cot\delta = -\frac{1}{a_1^{(3)}} + \frac{r_1^{(3)}p^2}{2} \Rightarrow \cot\delta(p_r) = -\frac{1}{a_1^{(3)}p_r^3} + \frac{r_1^{(3)}}{2p_r} = 0, \ \text{ and} \\ \frac{d}{dE}\cot\delta(E_r) = \frac{\mu}{p_r}\frac{d}{dp_r}\cot\delta(p_r) = -2/\Gamma_r \Rightarrow \frac{3}{a_1^{(3)}p_r^4} - \frac{r_1^{(3)}}{2p_r^2} = -\frac{2p_r}{\mu\Gamma_r}. \end{aligned} \tag{2.26}$$

For the resonance momentum and width, one gets (see also Refs. [19, 20, 60])

$$p_r^2 = \frac{2}{a_1^{(3)} r_1^{(3)}}\,, \qquad \text{and} \qquad \Gamma_r = -\frac{2p_r^3}{\mu r_1^{(3)}}\,. \tag{2.27}$$

Solving these equations results

$$a_1^{(3)} = -\frac{\mu\Gamma_r}{p_r^5}, \text{ and } r_1^{(3)} = -\frac{2p_r^3}{\mu\Gamma_r}. \tag{2.28}$$

$p_r = +\sqrt{2\mu E_r}$ is chosen so that ($a_1^{(3)}$and$r_1^{(3)}$) are negative to be consistent with the Wigner bound [61, 62]. If the experimental central values for $E_r = 0.222$ MeV and $\Gamma_r = 0.031$ MeV are taken in the c.m. frame we find $(|1/a_1^{(3)}|^{1/3}, r_1^{(3)}) = (46.38, -547.1)$ MeV, and from Eq (2.21) we are able to determine the EFT couplings.

To test the robustness of the above procedure, "synthetic data" for the resonance phase shifts from a known nuclear interaction are generated. A single-particle potential given by the Woods-Saxon form [39] is taken,

$$V(r) = -v_0 \left[1 + \exp\left(\frac{r - R_c}{a_c}\right)\right]^{-1} + \frac{1}{2}\frac{v_{so}}{r}\frac{d}{dr}\left[1 + \exp\left(\frac{r - R_c}{a_c}\right)\right]^{-1}, \tag{2.29}$$

where the $1/2$ factor in the second term comes from the expectation value of the single-particle spin-orbit operator in the $3^+$ channel. Natural units with $\hbar = 1 = c$ are used. In a study by Tombrello [38], the central potential with a depth $v_0 = 26.42$ MeV, spin-orbit $v_{so} = 0$, range $R_c = 2.95$ fm, and diffusiveness $a_c = 0.52$ fm was used to reproduce the resonance energy. A more recent work from Huang *et al.* [39] uses $v_0 = 34.93$ MeV, spin-orbit potential depth $v_{so} = 10$ MeV, $R_c = 2.391$ fm, and $a_c = 0.65$ fm. The two sets of parameters produce nearly identical phase shifts, Fig. 2.2. Plugging Huang's synthetic data into Eq. (2.24) generates $E_r = 0.228$ MeV and $\Gamma_r = 0.115$ MeV. From Eq. (2.28), one gets

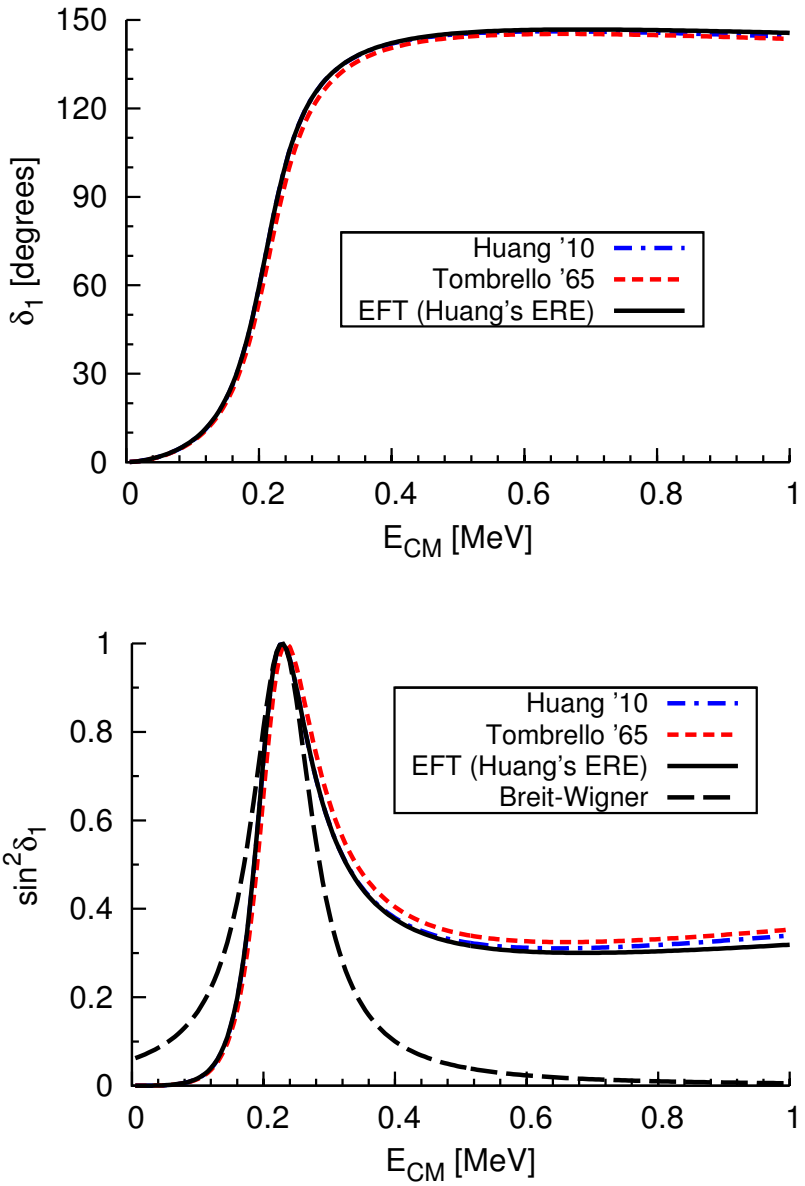


Figure 2.2

$^5P_3$ phase shifts of $^7\mathrm{Li}(n,\gamma)^8\mathrm{Li}$

Blue dot-dashed curve is from Huang's [39] Woods-Saxon parameters, red dashed curve is using Tombrello's [38] parameters, black solid curve from EFT fitted to Huang's "synthetic data", black long-dashed curve from Breit-Wigner form.

$(|1/a_1^{(3)}|^{1/3}, r_1^{(3)}) = (30.69, -154.3)$ MeV, which are then used as input to the EFT curve shown in Fig. 2.2. Alternatively, one can extract directly the ERE parameters from the low-energy behavior of the phase shifts. Table 2.1 shows the numbers of $(|1/a_1^{(3)}|^{1/3}, r_1^{(3)})$ from different models.

Table 2.1

Comparison of resonance parameters

| Model | $(\|1/a_1^{(3)}\|^{1/3}, r_1^{(3)})$ MeV |
|---|---|
| Tombrello's | (31.02,-157.6) |
| Huang's | (30.84,-158.9) |
| EFT(Huang's synthetic data) | (30.69,-154.3) |
| Experimental Data | (46.38, -547.1) |

The Breit-Wigner curve using the extracted resonance parameters is also shown. We can see that the procedure outlined allows EFT to reproduce well the synthetic data at low energy.

Further, the chosen potential model parameters give a resonance width that is about three times larger than the experimental value is also noted. To fit the resonance width to experimental data would require tuning yet another parameter (besides the potential depth) in the Woods-Saxon potential. In the EFT language, two operators are required to describe a shallow $p$-wave resonance at LO. The corresponding couplings $(\Delta^{(3)}, h^{(3)})$ are directly related to the two experimental data: $E_r$ and $\Gamma_r$.

## 2.2 Capture cross section

### 2.2.1 E1 capture

The $^7\mathrm{Li}(n,\gamma)^8\mathrm{Li}$ capture from $E = 0$ to about $0.15$ MeV total c.m. energy is almost entirely given by the E1 transition from initial $s$-waves. The dominant contribution goes directly to the $2^+$ ground state, with a small fraction (about 10%) going to the $1^+$ excited state.

The $^7\mathrm{Li}(n,\gamma)^8\mathrm{Li}$ cross section is calculated in the c.m. frame with $\boldsymbol{p}$ ($\boldsymbol{k}$), the core (photon) momentum, and $\hat{\boldsymbol{k}} \cdot \hat{\boldsymbol{p}} = \cos\theta$. The incoming momentum $p$ as well as the binding momenta for the ground and the excited states $\gamma^{(\eta)}$ are assumed to be of the order of the low-energy scale, *i.e.*, $p \sim \gamma^{(\eta)} \sim Q$. The photon at LO has $|\boldsymbol{k}| = k_0 \approx (p^2 + [\gamma^{(\eta)}]^2)/(2\mu)$ and the Mandelstam variable $s \approx (M_n + M_c)^2 = M^2$. The c.m. differential cross section is

$$\frac{d\sigma}{d\phi d\cos\theta} = \frac{1}{64\pi^2 s}\frac{|\boldsymbol{k}|}{|\boldsymbol{p}|}|\mathcal{M}|^2 \approx \frac{1}{64\pi^2 M^2}\frac{p^2 + [\gamma^{(\eta)}]^2}{2\mu p}|\mathcal{M}|^2, \tag{2.30}$$

where $\gamma^{(2^+)} \approx 57.8$ MeV and $\gamma^{(1^+)} \approx 41.6$ MeV for the $2^+$ and $1^+$ final states, respectively.

I quote the final result for capture to the $^5P_2$ state from Ref. [41] here for completeness. The diagrams in Fig. 2.3 shows the E1 capture to the ground state at LO. The photons are

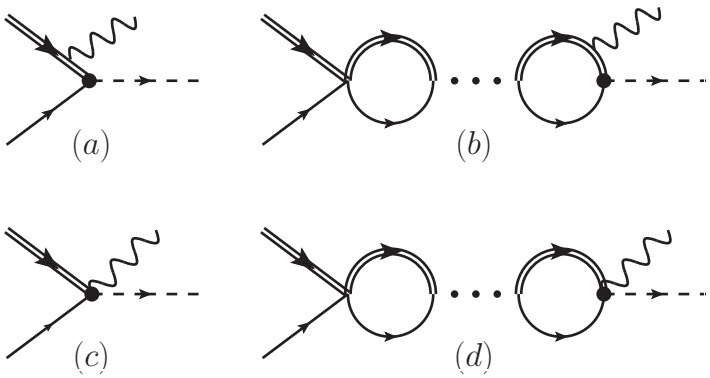


Figure 2.3

Capture reactions $^7\mathrm{Li}(n,\gamma)^8\mathrm{Li}$

Wavy lines represent photons. "$\cdots$" represents initial state $s$-wave interaction.

minimally coupled to the $^7$Li nucleus by gauging the core derivatives $\boldsymbol{\nabla}_C \to \boldsymbol{\nabla}_C + ieZ_c\boldsymbol{A}$ with $Z_c = 3$ as the core charge.

$$\begin{aligned}\left|\mathcal{M}_{\mathrm{E1}}^{(^5P_2)}\right|^2 &= 5\left(\frac{Z_cM_n}{M}\right)^2 \frac{64\pi\alpha M^2\left|h^{(2^+)}\sqrt{\mathcal{Z}^{(2^+)}}\right|^2}{\mu} \\ &\quad\times\left[|1+X|^2-\frac{p^2\sin^2\theta}{p^2+[\gamma^{(2^+)}]^2}\left(\frac{2[\gamma^{(2^+)}]^2}{p^2+[\gamma^{(2^+)}]^2}+X+X^*\right)\right], \qquad (2.31)\\ X &= \frac{1}{-1/a_0^{(2)}-ip}\left[\frac{2}{3}\frac{[\gamma^{(2^+)}]^3-ip^3}{[\gamma^{(2^+)}]^2+p^2}+ip\right],\end{aligned}$$

with $\alpha = e^2/(4\pi)$. The amplitude $\left|\mathcal{M}_{\mathrm{E1}}^{(^3P_2)}\right|$ is obtained from the above by replacing $a_0^{(2)}$ with $a_0^{(1)}$. The E1 transition to the $2^+$ ground state is written as

$$\frac{d\sigma_{\mathrm{E1}}^{(2^+)}}{d\cos\theta} = \frac{1}{32\pi M^2}\frac{p^2+[\gamma^{(2^+)}]^2}{2\mu p}\frac{1}{8}\frac{\left|\mathcal{M}_{\mathrm{E1}}^{(^5P_2)}\right|^2+\left|\mathcal{M}_{\mathrm{E1}}^{(^3P_2)}\right|^2}{2}, \qquad (2.32)$$

taking the $^8$Li ground state $|2^+\rangle$ as the symmetric combination of final states.

Integration over the angle $\theta$ gives the total cross section $\sigma(p)$ for an E1 transition . A common effective range parameter $r_1^{(2^+)}$ in $\mathcal{Z}^{(2^+)}$ is used as explained earlier, see Ref. [41]

for details. Fitting of the thermal cross section $\sigma^{(2^+)} = 40.56$ mb [44] gives $r_1^{(2^+)} = -1.47$ fm$^{-1}$, which is close to $r_1^{(2^+)} = -1.55$ fm$^{-1}$ value which can be obtained from the data in Ref [58]. In this work, the value obtained from the thermal capture will be used .

The E1 capture cross section to the $1^+$ excited state, $\sigma_{\rm E1}^{(1^+)}$, comprises the same set of diagrams in Fig. 2.3 except the final state dimer, which is in the $1^+$ state. The sum over the final polarization states gives an overall factor of 3 instead of 5. Therefore we have

$$\begin{aligned}
\left|\mathcal{M}_{\rm E1}^{(^5P_1)}\right|^2 &= 3\left(\frac{Z_c M_n}{M}\right)^2 \frac{64\pi\alpha M^2 \left|h^{(1^+)}\sqrt{\mathcal{Z}^{(1^+)}}\right|^2}{\mu} \\
&\quad \times \left[|1+Y|^2 - \frac{p^2\sin^2\theta}{p^2+[\gamma^{(1^+)}]^2}\left(\frac{2[\gamma^{(1^+)}]^2}{p^2+[\gamma^{(1^+)}]^2}+Y+Y^*\right)\right], \qquad (2.33) \\
Y &= \frac{1}{-1/a_0^{(2)} - ip}\left[\frac{2}{3}\frac{[\gamma^{(1^+)}]^3 - ip^3}{p^2+[\gamma^{(1^+)}]^2} + ip\right], \\
\frac{d\sigma_{\rm E1}^{(1^+)}}{d\cos\theta} &= \frac{1}{32\pi M^2}\frac{p^2+[\gamma^{(1^+)}]^2}{2\mu p}\frac{1}{8}\frac{\left|\mathcal{M}_{\rm E1}^{(^5P_1)}\right|^2 + \left|\mathcal{M}_{\rm E1}^{(^3P_1)}\right|^2}{2}, \qquad (2.34)
\end{aligned}$$

where the replacements $[h^{(2^+)}]^2\mathcal{Z}^{(2^+)} \to [h^{(1^+)}]^2\mathcal{Z}^{(1^+)}$, $\gamma^{(2^+)} \to \gamma^{(1^+)}$ are made in Eqs. (2.33, 2.34). The $|1^+\rangle$ state is considered to be the anti-symmetric combination of the final states. As in the $2^+$ case, the amplitude in the other spin channel $\left|\mathcal{M}_{\rm E1}^{(^3P_1)}\right|$ is derived from $a_0^{(2)} \to a_0^{(1)}$, with a common effective range parameter $r_1^{(1^+)}$. From the thermal capture rate $\sigma^{(1^+)} = 4.80$ mb to the $1^+$ state, $r_1^{(1^+)} \approx -1.93$ fm$^{-1}$ is obtained. The E1 capture cross section to the ground and excited state is shown in Fig. 2.4. The potential model results for comparison is also shown. The leading uncertainty in the potential model results seems to be associated with the poorly known effective range $r_1^{(2^+)}$ that we determine from the thermal capture rate. We also notice that the data set that we call ImhofB is more consistent with the $1/v$ behavior suggested by the Blackmon [58] and Lynn [44] data than ImhofA.

As seen in Fig. 2.4, E1 capture does not reproduce data at higher energy where the resonance occurs. In order to explain the resonance, M1 capture needs to be considered.

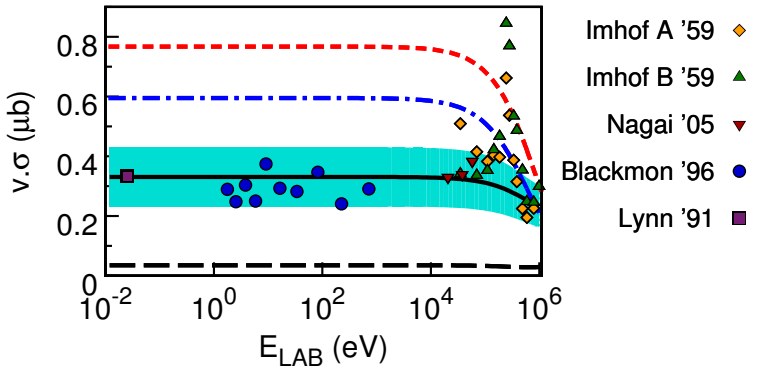


Figure 2.4

E1 capture of $^7\mathrm{Li}(n,\gamma)^8\mathrm{Li}$

Black long-dashed and solid curves are the EFT results for the E1 capture to the excited state and the total E1 capture, respectively. The shaded area shows the estimated $30\%$ EFT errors in the latter. The results of the potential model code CDXS+ [63] using parameters from Ref. [28] and Ref. [38] are given respectively by the blue dot-dashed and red dashed curves. The experimental points are from Refs. [64, 65, 58, 44]

### 2.2.2 M1 capture

Around $E \approx 200$ keV, the $3^+$ resonance enhances the cross section through an M1 transition to the ground state. The M1 capture proceeds through an initial $p$-wave state is considered, and therefore, is suppressed at low energies. In contrast, the E1 capture takes place via initial $s$-wave states. However, the presence of the $3^+$ resonance enhances the M1 contribution around the resonance energy, making it comparable to E1. In Fig. 2.5, the diagrams that make the leading contributions to the M1 capture are shown.

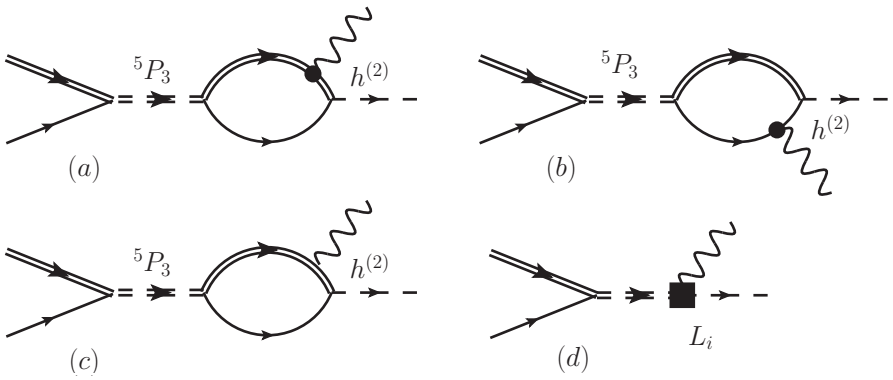


Figure 2.5

$3^+$ Resonance Capture of $^7\mathrm{Li}(n,\gamma)^8\mathrm{Li}$

The photon is coupled through the magnetic moment to the neutron (single solid line) and $^7$Li nucleus (double solid line). Single dashed line is the ground state $^8$Li $2^+$ dressed dimer, double dashed line is the $^8$Li $3^+$ resonance dressed dimer.

The first two Feynman diagrams show that the neutron and core magnetic moment couplings contribution to both $^5P_2$ and $^3P_2$ final states. In the third one, the magnetic photon couples to the charged $^7$Li core "in flight" or, in a more classical picture, to the electromagnetic current generated by the orbital motion of the charged $^7$Li core. It arises from minimal photon coupling and contributes only to the $^5P_2$ final state. The last diagram contains two-body currents in the respective $^5P_2$ and $^3P_2$ channels. Naively, counting only factors of $Q/\Lambda$, the contributions from two-body currents seem to be more important than the ones from the magnetic moments.

The diagrams in the final ${}^5P_2$ channel result in

$$i\mathcal{M}_{\rm M1}^{({}^5P_2)} = \epsilon_{abc}\varepsilon_{ij}^*\varepsilon_c^{(\gamma)*}G_{ijalmq}p_q k_b\, h^{(2^+)}\sqrt{2M\mathcal{Z}^{(2^+)}}\,\mu_N\left[-\frac{[h^{(3)}]^2}{2\pi\mu}D^{(3)}(p^2/2\mu,0)\right]\sqrt{3}$$
$$\times U_N^T(-\boldsymbol{p})Q_{lm}U_C(\boldsymbol{p})\left[\sqrt{\frac{3}{2}}\left(\frac{3}{2}g_c+\frac{1}{2}g_n+\frac{2\mu Z_c M_n}{M_c^2}\right)I(p;\lambda)-\frac{2\pi L^{(2)}}{h^{(3)}h^{(2^+)}}\right], \tag{2.35}$$

with

$$I(p;\lambda)=\frac{2}{3}\frac{[\gamma^{(2^+)}]^3-ip^3}{[\gamma^{(2^+)}]^2+p^2}-\lambda. \tag{2.36}$$

For the ${}^3P_2$ channel, one gets

$$i\mathcal{M}_{\rm M1}^{({}^3P_2)} = -\,i\epsilon_{abc}\varepsilon_{ij}^*\varepsilon_c^{(\gamma)*}G_{ijalmq}p_q k_b\, h^{(2^+)}\sqrt{2M\mathcal{Z}^{(2^+)}}\,\mu_N\left[-\frac{[h^{(3)}]^2}{2\pi\mu}D^{(3)}(p^2/2\mu,0)\right]\sqrt{3}$$
$$\times U_N^T(-\boldsymbol{p})Q_{lm}U_C(\boldsymbol{p})\left[\sqrt{\frac{3}{2}}\left(\frac{3}{2}g_c-\frac{3}{2}g_n\right)I(p;\lambda)-\frac{2\pi L^{(1)}}{h^{(3)}h^{(2^+)}}\right]. \tag{2.37}$$

Numerically the gyromagnetic factors are $\sqrt{3/2}(3g_c/2+g_n/2+2\mu Z_c M_n/M_c^2)\sim 1.8$ for ${}^5P_2$ and $\sqrt{3/2}(3g_c/2-3g_n/2)\sim 11$ for ${}^3P_2$. The former is of natural size for a dimensionless constant: in Eq. (2.35), the two-body current dominates for a natural $L^{(2)}\sim 1$ and the loop contribution is subleading. However, the ${}^3P_2$ numerical factor is large and enhances the loop contribution beyond the estimates of the power counting. Thus in Eq. (2.37), the loop contribution is as important as the two-body current and both enter at leading order. For convenience, the loop contribution and two-body magnetic coupling are kept at the same order in both the spin channels. The dependence on the renormalization scale $\lambda$ coming from the loop function $I(p,\lambda)$, Eqs. (2.35), (2.37), is then cancelled by the

two-body couplings $L^{(1)}$ and $L^{(2)}$, respectively.

One can write

$$\begin{aligned} L^{(2)} &= -\frac{h^{(3)}h^{(2)}}{2\pi}\left[\sqrt{\frac{3}{2}}\left(\frac{3}{2}g_c+\frac{1}{2}g_n+\frac{2\mu Z_c M_n}{M_c^2}\right)\lambda+\beta^{(2)}\right], \\ L^{(1)} &= -\frac{h^{(3)}h^{(2)}}{2\pi}\left[\sqrt{\frac{3}{2}}\left(\frac{3}{2}g_c-\frac{3}{2}g_n\right)\lambda+\beta^{(1)}\right], \end{aligned} \tag{2.38}$$

where $\beta^{(i)}$'s are renormalized two-body parameters with dimensions of mass.

Then the total cross section for M1 capture can be written as

$$\begin{aligned} \sigma_{\rm M1}^{(2^+)} &= \frac{1}{14}\frac{7}{3}\frac{\alpha\mu}{M_p^2}[h^{(2^+)}]^2\left|\mathcal{Z}^{(2^+)}\right|\frac{(p^2+[\gamma^{(2^+)}]^2)^3}{(2\mu p)^3}\left|\frac{p^2}{-1/a_1^{(3)}+\frac{1}{2}r_1^{(3)}p^2-ip^3}\right|^2 \\ &\times\left\{\left|\sqrt{\frac{2}{3}}\left(\frac{3}{2}g_c+\frac{1}{2}g_n+\frac{2\mu Z_c M_n}{M_c^2}\right)\frac{[\gamma^{(2^+)}]^3-ip^3}{[\gamma^{(2^+)}]^2+p^2}+\beta^{(2)}\right|^2\right. \\ &\left.+\left|\sqrt{\frac{2}{3}}\left(\frac{3}{2}g_c-\frac{3}{2}g_n\right)\frac{[\gamma^{(2^+)}]^3-ip^3}{[\gamma^{(2^+)}]^2+p^2}+\beta^{(1)}\right|^2\right\}, \end{aligned} \tag{2.39}$$

where the proton mass $M_p = 938.3$ MeV is used. We summed over the final state dimer and photon polarizations, and averaged over the initial spin states. Introduced photon vectors ($\varepsilon_i^{(\gamma)}$), spin-1 ($\varepsilon_j$), spin-2 ($\varepsilon_{ij}$) and spin-3 tensor ($\varepsilon_{ijk}$) polarizations obey the following sums [47, 48]

$$\sum_{\rm pol.}\varepsilon_i^{(\gamma)}\varepsilon_j^{(\gamma)*} = \delta_{ij}-\frac{k_i k_j}{k^2}\,,\ \sum_{\rm pol.avg.}\varepsilon_i\varepsilon_j^* = \frac{\delta_{ij}}{3}\,,\ \sum_{\rm pol.avg.}\varepsilon_{ij}\varepsilon_{lm}^* = \frac{R_{ijlm}}{5}\,, \tag{2.40}$$

$$\sum_{\rm pol.avg.}\varepsilon_{ijk}\varepsilon_{lmq}^* = \frac{G_{ijklmq}}{7}\,. \tag{2.41}$$

The magnetic moment and orbital momentum weights are easy to understand if one compares with the non-relativistic quantum operator in the M1 transition, which is proportional to

$$\left(\frac{\mu M_n Z_c}{M_c^2}\vec{\boldsymbol{L}}+g_c\vec{\boldsymbol{S}}_C+g_n\vec{\boldsymbol{S}}_N\right)_z\,, \tag{2.42}$$

and its expectation value between the initial ${}^5P_3$ state and the final ${}^5P_2$ and ${}^3P_2$ states, respectively.

Now we have expressions for cross sections of both E1 and M1 capture. *A priori* estimation of the size of the couplings is important before fit expressions to the data. In the Section. 2.3, I will present the details of the power counting for producing shallow bound state and power counting for two body current in E1 and M1 capture.

## 2.3 Choosing the appropriate power counting

### 2.3.1 Producing a shallow ($p$-wave) bound or virtual state

In this section I present the details of the power counting, starting with the $p$-wave elastic channel. This also allows one to estimate the expansion parameter $Q/\Lambda$. It has been shown earlier that the contribution of the two-body currents relative to the loop diagrams in M1 capture scales as $L^{(i)}/(g_{[i]}Qh^{(3)}h^{(2)})$, where $g_{[i]}$ is a combination of the gyromagnetic ratios $g_c$, $g_n$ that is of natural size in the ${}^5P_2$ channel, but large in the ${}^3P_2$ channel. To estimate the size of two-body currents, estimates for $h^{(\eta)}$ is also needed that is related to the effective range. In Section. 2.1 we have fitted the ERE parameters $a_1^{(\eta)}$, $r_1^{(\eta)}$ in their respective $p$-channels. We found $\left|1/a_1^{(\eta)}\right|^{1/3} \sim 30-50$ MeV and $r_1^{(\eta)}/2 \sim 100-250$ MeV. This is consistent with the situation in Ref. [18], where only $1/a_1^{(\eta)}$ is fine-tuned to scale as $\Lambda Q^2$ while $r_1^{(\eta)} \sim \Lambda$ obeys the naive expectation. Then in the EFT matching conditions, Eq. (2.21),

$$
\begin{aligned}
-\frac{\pi}{[h^{(\eta)}]^2} &= \frac{1}{2}r_1^{(\eta)} + \frac{3}{2}\lambda, \\
-\frac{2\pi\mu\Delta^{(\eta)}}{[h^{(\eta)}]^2} &= -1/a_1^{(\eta)} + \frac{\pi}{2}\lambda^3,
\end{aligned}
$$

the renormalization scale $\lambda \sim Q$ from the loop momentum is a higher order contribution in a $Q/\Lambda$ expansion. To obtain $[h^{(\eta)}]^2 = -2\pi/r_1^{(\eta)} \sim 1/\Lambda$ and $\mu\Delta^{(\eta)} = -1/(r_1^{(\eta)} a_1^{(\eta)}) \sim Q^2$ the dimer propagator is expand as

$$D(p_0, \boldsymbol{p}) = D_{-2}(p_0, \boldsymbol{p}) + D_{-1}(p_0, \boldsymbol{p}) + \cdots , \tag{2.43}$$

and the LO term is given by the bare propagator,

$$D_{-2}(p_0, \boldsymbol{p}) = \frac{1}{\Delta - \zeta^2/(2\mu)},$$

since loop contributions enter at higher orders. The subscript indicates the scaling with powers of $Q$ and we have suppressed the superscript $\eta$ here and in the rest of this section. To renormalize the loop expansion systematically we write the couplings as [55, 66]

$$\begin{aligned} h &= h_0 + h_1 + \cdots , \\ \Delta &= \Delta_2 + \Delta_3 + \cdots , \end{aligned} \tag{2.44}$$

stressing again that the subscripts indicate the powers in $Q$. Matching to the ERE we get

$$\begin{aligned} -\frac{\pi}{h_0^2} &= \frac{1}{2} r_1, & 2\pi \frac{h_1}{h_0^3} &= \frac{3}{2}\lambda, \\ \Delta_2 &= -\frac{1}{\mu r_1 a_1}, & \Delta_3 &= \frac{\pi}{2\mu r_1}\lambda^3 + \frac{3}{\mu r_1^2 a_1}\lambda. \end{aligned} \tag{2.45}$$

At next-to-leading order (NLO), the dimer propagator gets a contribution from the one-loop self-energy diagram

$$\begin{aligned} D_{-1}(p_0, \boldsymbol{p}) &= [iD_{-2}(p_0, \boldsymbol{p})]^2 \Sigma(p_0, \boldsymbol{p}), \\ i\Sigma(p_0, \boldsymbol{p}) &= i\frac{2h_0^2}{\mu} f_1(p_0, \boldsymbol{p}) + i\Delta_3 = i\frac{h_0^2}{2\pi}\zeta^3 - i\frac{3h_0^2}{4\pi\mu}\lambda\zeta^2 + i\frac{h_0^2}{4\mu}\lambda^3 + i\Delta_3 \\ &= -i\frac{\zeta^3}{r_1} + i\frac{3\zeta^2\lambda}{2\mu r_1} + \frac{3\lambda}{\mu r_1^2 a_1}, \end{aligned} \tag{2.46}$$

which is a $\lambda$-dependent result. However, the elastic amplitude in Eq. (2.19)

$$\begin{aligned} A(p) =& - h^2 \frac{p^2}{\mu^2} D(\frac{p^2}{2\mu}, 0) \\ \approx& - h_0^2 \frac{p^2}{\mu^2} D_{-2}(\frac{p^2}{2\mu}, 0) - h_0^2 \frac{p^2}{\mu^2} D_{-2}(\frac{p^2}{2\mu}, 0) \left[ D_{-1}(\frac{p^2}{2\mu}, 0)/D_{-2}(\frac{p^2}{2\mu}, 0) + \frac{2h_1}{h_0} \right] \\ =& \frac{2\pi}{\mu} \frac{p^2}{-1/a_1 + \frac{1}{2} r_1 p^2} \left( 1 + \frac{ip^3}{-1/a_1 + \frac{1}{2} r_1 p^2} \right), \end{aligned} \tag{2.47}$$

is $\lambda$-independent as expected for a physical observable. This is in agreement with the expansion of the ERE amplitude up to NLO in $Q/\Lambda$. At LO, the binding momentum is given by $\gamma = \sqrt{-2/(r_1 a_1)}$. The NLO term introduces a double pole which, at least formally, is suppressed in the $Q/\Lambda$ expansion. To treat the bound state consistently we rewrite the $p$-wave ERE expansion [55, 66] as

$$p^3 \cot \delta(p) = \gamma^3 + \frac{1}{2} s (p^2 + \gamma^2) + \cdots . \tag{2.48}$$

From Eqs. 2.13 and 2.48,

$$\begin{aligned} -1/a_1 =& \gamma^3 + \frac{1}{2} s \gamma^2 + \cdots , \\ r_1 =& s + \cdots , \end{aligned} \tag{2.49}$$

and define the EFT couplings as

$$\begin{aligned} -\frac{\pi}{h_0^2} &= \frac{1}{2} r_1, & 2\pi \frac{h_1}{h_0^3} &= \frac{3}{2} \lambda, \\ \Delta_2 &= \frac{\gamma^2}{2\mu}, & \Delta_3 &= \frac{\pi}{2\mu r_1} \lambda^3 - \frac{3\gamma^2}{2\mu r_1} \lambda + \frac{\gamma^3}{\mu r_1}. \end{aligned} \tag{2.50}$$

The amplitude is now written as

$$A(p) = \frac{2\pi}{\mu} \frac{2p^2}{r_1(\gamma + ip)(\gamma - ip)} \left[ 1 + 2 \frac{p^2 + ip\gamma - \gamma^2}{r_1(\gamma - ip)} \right], \tag{2.51}$$

where the NLO correction contributes a factor of $-3\gamma/r_1$ to the residue at the pole $p = i\gamma$ without introducing any spurious double pole. This correction to the residue at the pole is consistent with the wave function renormalization calculated earlier

$$h^2\mathcal{Z} = -\frac{2\pi}{3\gamma + r_1}. \tag{2.52}$$

The complete result is kept instead of expanding. A convenient approach to recover the complete result at NLO without resummation is to use the so called "zed"-parameterization [67]. In this approach, one would define, for example, $h_0^2 = -2\pi(\mathcal{Z}-1)/(3\gamma)$, $h_1 = 3h_0^3\lambda/(4\pi)$ and recover, for the wave function renormalization,

$$\mathcal{Z} = 1 + (\mathcal{Z}-1) + 0 + 0 + \cdots, \tag{2.53}$$

where $\mathcal{Z} - 1 \sim Q$ is treated as a perturbation, see Ref. [67] for details. Here simply use the resummed result for the $2^+$ bound state and the $1^+$ excited state.

In the case of low-lying resonance, in addition to the above power counting, an additional fine-tuning applies. That is purely kinematical and is discussed in Refs. [18, 56]. This second fine-tuning requires the loop contribution to be treated non-perturbatively at energies near resonance. Since energies near the resonance is considred in our capture calculations, the loop contributions are resumed in the $3^+$ initial state.

### 2.3.2 Scaling of the two-body currents in the E1 capture

The two-body currents appear in M1 capture as $L/(g_{[i]}Qh^2)$. Since $h^2 \sim 1/\Lambda$ as shown above, the relative contribution for a natural two-body current scales as $\Lambda/(g_{[i]}Q)$. At LO and from the specific numerical values of $g_{[i]}$, one notices that in the ${}^5P_2$ channel, only

the two-body current enters, while in the ${}^3P_2$ case, both two-body and one-body (magnetic moment) currents contribute. In principle, for a systematic treatment, one could write $\beta^{(2)} = \beta_0^{(2)} + \beta_1^{(2)} + \cdots$ and perform perturbative renormalization outlined above for the ${}^5P_2$ channel, while keeping the full loop contribution in the ${}^3P_2$ channel. We verified that such a treatment satisfies the power counting estimates. As mentioned in Section. 2.2, we keep the loop contribution at LO in both ${}^3P_2$ and ${}^5P_2$ channels for convenience.

### 2.3.3 Scaling of the two-body currents in the M1 capture

The scaling of two-body currents that appear in the E1 case is different than in M1 capture. To keep the discussion fairly general, let me introduce a dimer field $\pi^{(s-\text{wave})}$ for the two initial state $s$-wave channels ${}^5S_2$, ${}^3S_1$. Then the relative contribution of the two-body to one-body current in the E1 capture is generically $L_{\text{E1}} k_0 \mu h^{(s-\text{wave})}/[h\Delta^{(s-\text{wave})}]$, where the operator $eL_{\text{E1}}\phi_{ij}^\dagger E_x \pi_{yz} T_{xyzij}$ is considered for a transition from ${}^5S_2$ to the ${}^5P_2$ ground state, for illustration. $h^{(s-\text{wave})} \sim h$ is the $\pi$-nucleon-core coupling and $\Delta^{(s-\text{wave})}$ the dimer propagator in the $s$-wave. In the power counting, one either takes $\Delta^{(s-\text{wave})} \sim \Lambda$ to treat $s$-wave interaction as perturbative as would be the case for small natural-sized scattering length (the ${}^3S_1$ channel for momenta $p \lesssim 227$ MeV) or take $\Delta^{(s-\text{wave})} \sim Q$ to treat $s$-wave interaction as non-perturbative as would be the case for large unnatural-sized scattering length (the ${}^5S_2$ channel around $p \sim 54$ MeV). For a natural $L_{\text{E1}}$ given by dimensional analysis, the relative contribution $L_{\text{E1}} k_0 \mu h^{(s-\text{wave})}/[h\Delta^{(s-\text{wave})}]$ scales as either $Q^2$ for perturbative or as $Q$ for non-perturbative $s$-wave interaction in the initial state. The former is a N$^2$LO contribution whereas the latter is a NLO contribution. One can use

the estimated power counting to identify the LO contribution of the total cross section. The unknown parameters $\beta^{(1)}$ and$\beta^{(2)}$ need to be found by fitting the data. In the section 2.4 the LO result will be discussed.

## 2.4 Results and Discussion

As seen in the Eq. (2.39), the total M1 capture cross section depends on two parameters $\beta^{(1)}$, $\beta^{(2)}$, that fit to capture data near resonance. The EFT couplings $(\Delta^{(3)}, h^{(3)})$ are directly related to the known resonance energy (position) and width of the resonance in the ${}^5P_3$ elastic channel. Only the amplitude of the cross section near the resonance depends on the values of $\beta^{(i)}$s, but not its position or width. If one follows the power counting naively, then only the two-body currents contribute to LO, and the two $\beta^{(i)}$s are correlated. In the resummed amplitude show a similar behavior in our fits. Thus we use a common $\beta = \beta^{(1)} = \beta^{(2)}$.

Fitting the ImhofB [64] with the the experimental $3^+$ width results in' $\beta = 170$ MeV. Moreover, a fit to the same data set, but with the $3^+$ width extracted from Huang's potential model phase shift provides $\beta = 83$ MeV. $\beta$ is $/o0 - -44$ MeV when fit data set ImhofA with Huang's $3^+$ width. The results are shown in Fig. 2.6 and Fig. 2.7. Note that the authors assign a $20\%$ error to data sets ImhofA and ImhofB [64]. This means away from the resonance where the cross section is small, the errors are also small. This makes the region where the resonance contributes the most, the least constraining in the fits.

According to Fig. 2.7, the fit with a wider resonance, $\Gamma_r = 0.11$ MeV, seems to describe the data better than using the experimental width $\Gamma_r = 0.031$ MeV. Smaller error bars

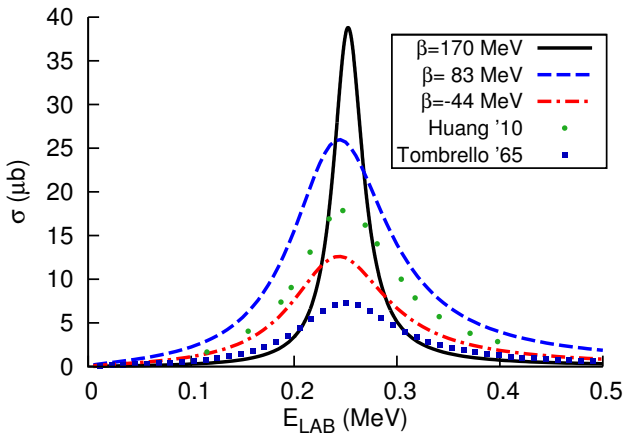


Figure 2.6

M1 capture of $^7\mathrm{Li}(n,\gamma)^8\mathrm{Li}$

Black curve with $\beta = 170$ MeV, resonance energy and width fitted to experimental data. Blue dashed curve with $\beta = 83$ MeV, red dot-dashed curve with $\beta = -44$ MeV, resonance energy and width fitted to Huang's potential model. Green circles are results from Huang *et al.*, blue squares M1 capture using Tombrello's potential model using code CDXS+.

near resonance than the estimated $20\%$ ones could be useful to make stronger statements. Higher order EFT corrections estimated to be around $30\%$ could also make the fit better, even with the narrower experimental width. With these considerations in mind, one sees that with the current data, the LO EFT does not reproduce the width seen in capture. This could be an indication of the limitation of the single-particle approximation to describe the capture reaction near resonance energy as it is towards the higher momenta region of the domain of applicability of the low-energy EFT. Nonetheless, the same feature is observed in the microscopic calculation of Ref. [34]. Potential models provide a wider width by coincidence and the caudated width is not in agreement with the experimental value $\Gamma_r = 0.031$ MeV.

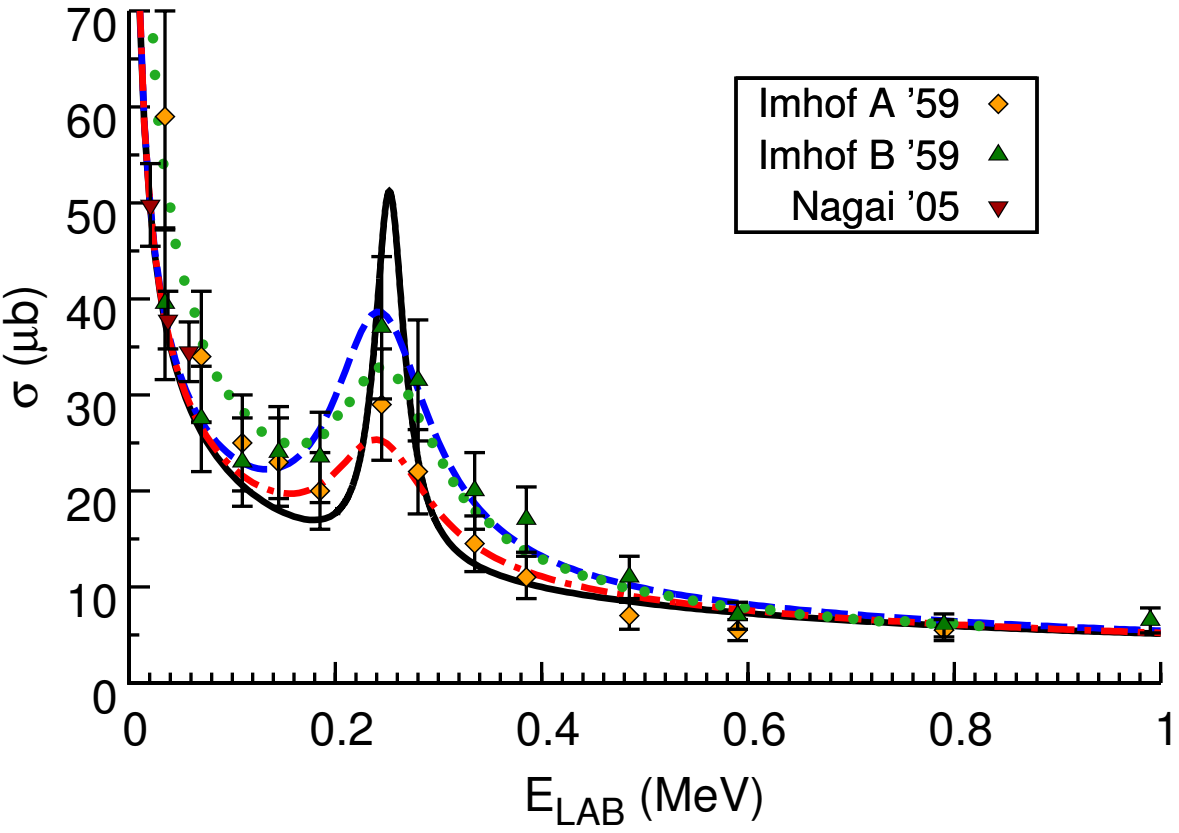


Figure 2.7

Capture cross section including E1 and M1 transitions

$r_1^{(2^+)} = -1.47$ fm$^{-1}$, $r_1^{(1^+)} = -1.93$ fm$^{-1}$ are used. Black solid curve with $\beta = 170$ MeV and experimental resonance width, blue dashed curve $\beta = 83$ MeV, red dot-dashed curve with $\beta = -44$ MeV, and Huang's potential model resonance width. Green dots are results from Huang *et al.* The experimental points are from Refs. [64, 65, 58, 44].

To expand the range of applicability of the EFT to slightly higher momenta, one needs to include other missing degrees of freedom. The $\frac{1}{2}^-$ excited state of the $^7$Li core ($^7\mathrm{Li}^*$), which contributes only to the spin-1 channel, is the first to consider. It can be incorporated explicitly in the present halo EFT, since its energy remains close to the core ground state ($\sim$ 0.5 MeV) and far from the first breakup channel ($\sim$ 2.5 MeV). In the $n$-$^7$Li c.m. system, the energy required to probe $^7\mathrm{Li}^*$ involves momenta of $\sim$ 80 MeV. In the present work, the higher incoming momentum considered is $\sim$ 40 MeV, which justifies having the $^7\mathrm{Li}^*$ "integrated out". An analogous situation is the Delta resonance in chiral perturbation theory (the EFT for pions and nucleons) where the Delta can be integrated out of the theory when the energy relative to the pion-nucleon threshold is smaller than the nucleon-Delta mass splitting [56, 60, 68]. Further, it can also be shown that the virtual contributions of $^7\mathrm{Li}^*$ to the ground state of $^8$Li in the neutron capture reaction is a subleading effect.

Contributions from $d$-waves to the E1 transition, which are in principle suppressed by a factor of $(Q/\Lambda)^4$, may also become relevant with increasing energy [28], depending on the desired accuracy. The next level of sophistication is the inclusion of alpha and triton degrees of freedom in a three-cluster treatment, which should improve the description of the M1 capture reaction [35, 36, 37, 29].

## 2.5 Summary

As an extension of previous work, here the complete E1 transition at leading order is included, as well as the leading M1 capture of the $^7\mathrm{Li}(n,\gamma)^8\mathrm{Li}$ capture reaction at low energies. This model-independent EFT calculation results quantify the current uncertainties

in nuclear theory in the single-particle approximation, therefore serving as a guide to its limitations and also highlighting where more precise experimental input is necessary for improvements.

The E1 capture from $s$-waves to the excited state in $^8$Li is included explicitly pthat contributes about $10\%$ to the cross section at very low energy. The new EFT coupling constants associated with this process are completely determined by the binding energy of the excited state and the E1 thermal capture rate by the excited state [44]. For energies below $100$ keV, our results show the expected $1/v$ behavior also seen in potential models; however, they differ by a sizable overall normalization factor, directly related to the effective range in the ground state channel $r_1^{(2^+)}$. This is the dominant source of uncertainty in this low-energy region, and it could be determined from accurate elastic scattering data and partial wave analysis, but due to the present lack of the latter, it is poorly known. A fit to E1 thermal capture data gives $r_1^{(2^+)} \approx -1.47$ fm$^{-1}$; see also Ref. [41].

M1 capture proceeds via the $3^+$ resonance near $E \sim 0.2$ MeV in the $^5P_3$ channel. It is suppressed at very low momentum due to the $p$-wave initial state. However, near resonance there is an enhanced contribution to the total cross section that needs to be considered. In the halo EFT approach, the size of one-body (magnetic moment and orbital momentum couplings) and two-body currents that enter in to the calculation are included and estimated. The one-body current contribution is consistent with an effective magnetic dipole operator used in potential models, but the two-body currents are new ingredients. These latter also renormalize they loop contributions, and the corresponding couplings $\beta^{(1)}$ and $\beta^{(2)}$ are our free parameters to be determined from the capture data. The power

counting for two-body currents was studied, and found to contribute at LO and N$^2$LO in M1 and E1 capture, respectively.

The available capture data near resonance have large errors that hamper the quality of the fit. However, given the current data near resonance, it seems that using the experimental resonance width $\Gamma_r = 31$ keV in the $3^+$ elastic amplitude does a poor job in describing M1 capture data. This was also observed in the microscopic calculation of Ref. [34]. A significantly larger width, about three times the experimental one, provides much better fits. This is roughly the width that one gets in potential models that are tuned to the resonance energy. This is a coincidence since, in principle, one should tune the potential models to reproduce accurately not only the resonance energy $E_r$, but also the resonance width $\Gamma_r$. In the EFT formalism, the $p$-wave resonance requires two operators at LO that can be fixed by matching to the resonance energy and width. The fact that halo EFT is able to describe the resonance scattering (as shown in Section 2.1.2.2), but not to reproduce M1 capture might indicate the limitation of the current approach. As mentioned in Section 2.2, M1 capture could be on the outer edge of the range of applicability.

Nevertheless, the apparent discrepancy in the input related to the $3^+$ resonance width that is used in the ${}^5P_3$ elastic scattering and M1 capture reaction is unlikely to be resolved with current experimental information. More precise capture data around $0.22$ MeV (where M1 capture dominates) is needed to conclusively state if the single-particle approximation is sufficient to describe M1 capture in ${}^7\mathrm{Li}(n,\gamma){}^8\mathrm{Li}$.

# CHAPTER 3

# THE RADIATIVE CAPTURE OF NEUTRON ON CARBON-14

In this chapter I study another important halo nuclei interaction, $^{14}\mathrm{C}(n,\gamma)^{15}\mathrm{C}$ . The CNO cycle is one of the main energy sources in the helium burning layer of asymptotic giant branch stars and in the core helium burning of massive stars [12]. Like the reaction $^{7}\mathrm{Li}(n,\gamma)^{8}\mathrm{Li}$ , $^{14}\mathrm{C}(n,\gamma)^{15}\mathrm{C}$ is also a part of a CNO cycle which plays an important role in astrophysics. It is the slowest reaction in the cycle which leads to a substantial enrichment in $^{14}$C abundance [12]. In astrophysical scenarios, such as inhomogeneous Big Bang Nucleosynthesis (BBN), the slow $^{14}\mathrm{C}(n,\gamma)^{15}\mathrm{C}$ reaction limits the flow of the production of heavier nuclei $A > 14$ and the cross section of the reaction mainly depends on the p-wave direct capture to the ground state [69, 70].

Both direct capture experiments [71, 72, 73] and indirect Coulomb dissociation experiments [74, 75, 76, 77] provide cross sections of $^{14}\mathrm{C}(n,\gamma)^{15}\mathrm{C}$ at low energies. Coulomb dissociation is an alternate method to estimate the direct capture reactions involving radioactive isotopes that are often difficult to measure experimentally. In Coulomb dissociation experiments, it is required to carefully treat both parent $^{15}$C and daughter $^{14}$C nuclei in a strong Coulomb field of a heavy nucleus in addition to the nuclear interactions [78, 79, 80]. Theoretical calculations on $^{14}\mathrm{C}(n,\gamma)^{15}\mathrm{C}$ provides an opportunity to compare and contrast the capture rates that are obtained from direct capture measurements

and Coulomb dissociation data [81, 79]. This reaction has been calculated previously by other theoretical formulations, such as Refs. [69, 79, 39, 82]. In this work, the radiative capture $^{14}\mathrm{C}(n,\gamma)^{15}\mathrm{C}$ cross section is calculated at low-energies using halo EFT [17, 18].

Center-of-mass (c.m.) energies $\lesssim 2$ MeV is considered, corresponding to momenta $p \lesssim 60$ MeV, that is below the threshold for the excited states of $^{14}$C nucleus (or neutron). As in the EFT, the neutron and $^{14}$C core are treated as inert point-like particles. The ground state of $^{15}$C, identified as $J^\pi = \frac{1}{2}^+$, has a neutron separation energy $B$ of only $1.218$ MeV that corresponds to a binding momenta of $\gamma = \sqrt{2\mu B} \approx 46.21$ MeV, where $\mu$ is the neutron-$^{14}$C reduced mass. In nuclear structure calculations, the ground state of $^{15}$C can be considered as a single neutron halo bound to a $^{14}$C core. Then in the single-particle approximation, it is described as a $^2S_{1/2}$ state of $n + {}^{14}$C. The momenta $p$, $\gamma$ are associated with the soft scale $Q$. The energy threshold for the excited states of $^{14}$C, pion physics, etc., is identified with the hard scale $\Lambda \sim 100 - 200$ MeV.

The chapter is organized as follows: In Section 3.1, I introduce the basic theory and the interactions necessary for the $^{14}\mathrm{C}(n,\gamma)^{15}\mathrm{C}$ cross section calculation. The Lagrangian for the $s$- and $p$-wave interactions of neutron and carbon-14 are presented. In Section 3.2, I describe how the EFT couplings can be constrained from data. The E1 capture cross section is calculated in Section 3.3. Here both direct capture and Coulomb dissociation data are considered. EFT couplings are constrained to reproduce the available data. In Section 3.4, I analyze and formulate a power counting for estimating the sizes of the couplings and the various EFT contributions. Finally, Section 3.5 provides a summary of our work.

## 3.1 Formalism

The construction of the EFT for $^{14}\mathrm{C}(n,\gamma)^{15}\mathrm{C}$ requires description of the $n$+$^{14}$C bound state in the $^2S_{1/2}$ channel, and the initial state interaction of $n$+$^{14}$C in the $^2P_{1/2}$ and $^2P_{3/2}$ channels.

At low energies which are of interest, capture from lower partial wave initial states, such as $s$- and $p$-wave states, should dominate. The lowest multipole transition from the initial $p$-wave states $^2P_{1/2}$ and $^2P_{3/2}$ to the ground state $^2S_{1/2}$ is through E1 transitions. Neutron capture from initial $s$-wave state to the ground state through a M1 transition is suppressed (at one-body current level) due to the orthogonality of the continuum and bound state wave functions. There is a possibility of a transition from the initial $s$-wave and $p$-wave states to the excited state of $^{15}$C $J^\pi = \frac{5}{2}^+$; however, the transition has been found to be a small contribution to the total capture rate [69, 82, 83]. In this calculation, only the dominant effects are concentrated, so such small contributions are ignored.

In the following subsections the interaction Lagrangians for the $s$- wave and $p$-wave are constructed, respectively.

### 3.1.1 $s$-wave interaction

The interaction in the $^2S_{1/2}$ channel is written as

$$\mathcal{L}_s = \phi_\alpha^\dagger \left[ \Delta^{(0)} + i\partial_0 + \frac{\nabla^2}{2M} \right] \phi_\alpha + h^{(0)} \left[ \phi_\alpha^\dagger (N_\alpha C) + \mathrm{h.\,c.} \right], \tag{3.1}$$

where $\phi_\alpha$ is an auxiliary field with a spin index $\alpha$, $N_\alpha$ is the neutron field and $C$ is the carbon-14 scalar field. $M = M_n + M_c$ with neutron mass $M_n = 939.6$ MeV and $^{14}$C core mass $M_c = 13044$ MeV. Using the equation of motion for the $\phi$ field, it can be integrated

out of the theory in Eq. (3.1), and the interaction Lagrangian is written entirely in terms of four-particle neutron carbon-14 interactions.

### 3.1.2 $p$-wave interaction

Here, a Galilean invariant form consisting of the relative neutron and $^{14}$C core velocity $\boldsymbol{v}_C - \boldsymbol{v}_N$ , the neutron field $N_\alpha$, and the scalar carbon-14 field $C$ is considered in order to describe the initial $^2P_{1/2}$ and $^2P_{3/2}$ states. In particular we want to project a generic tensor $\psi_i^\alpha$, with a vector index $i = 1, 2, 3$ for the $p$-wave and a spin index $\alpha = 1, 2$ for the neutron spin, into the total angular momentum $J = 1/2$ piece and $J = 3/2$ piece. This can be done as

$$\psi_i^\alpha = \frac{1}{3}(\sigma_i\sigma_j)^{\alpha\beta}\psi_j^\beta + \left[\delta_{ij}\delta^{\alpha\beta} - \frac{1}{3}(\sigma_i\sigma_j)^{\alpha\beta}\right]\psi_j^\beta, \tag{3.2}$$

where the two pieces are irreducible forms representing the $^2P_{1/2}$ and $^2P_{3/2}$ states, respectively. $\sigma_i$ are the Pauli matrices. Thus the $p$-wave interaction in the EFT can be written as

$$\mathcal{L}_p = \chi_i^{\alpha,\eta\dagger}\left[\Delta^{(\eta)} + i\partial_0 + \frac{\nabla^2}{2M}\right]\chi_i^{\alpha,\eta} + \sqrt{3}h^{(\eta)}[\chi_i^{\alpha,\eta\dagger}P_{ik}^{\alpha\gamma,\eta}N_\gamma\left(\frac{\overrightarrow{\nabla}}{M_c} - \frac{\overleftarrow{\nabla}}{M_n}\right)_k C + \text{h. c}], \tag{3.3}$$

where $\eta = 1, 2$ corresponds to the $^2P_{1/2}$ and $^2P_{3/2}$ channels, respectively. These particular $p$-wave channels in $^{11}$Be were also studied in Refs. [23, 24]. The auxiliary field $\chi_i^\alpha$ in $p$-wave plays a role similar to the $\phi_\alpha$ field in the $s$-wave earlier in Eq. (3.1). The projectors $P_{ij}^{\alpha\beta,\eta}$ in Eq. (3.3) are

$$P_{ij}^{\alpha\beta,1} = \frac{1}{3}(\sigma_i\sigma_j)^{\alpha\beta}, \tag{3.4}$$
$$P_{ij}^{\alpha\beta,2} = \delta_{ij}\delta^{\alpha\beta} - \frac{1}{3}(\sigma_i\sigma_j)^{\alpha\beta}.$$

We have Lagrangians for both $s$-wave and $p$-wave. In the next session I describe the power counting for both waves.

## 3.2 Determining the EFT couplings

### 3.2.1 Elastic scattering parameters of $s$-wave

The non-relativistic $s$-wave ($\ell$=0) amplitude is calculated from the diagrams in Fig. 3.1. We get

$$i\mathcal{A}_0(p) = -ih_0^2 D_\phi(\frac{p^2}{2\mu}, 0), = -\frac{i[h^{(0)}]^2}{\Delta^{(0)} + p^2/(2\mu) + \mu[h^{(0)}]^2(\lambda + ip)/(2\pi)}, \tag{3.5}$$

where the dressed $\phi$ propagator is

$$\begin{aligned} iD_\phi(p_0, \boldsymbol{p}) =& \frac{i}{\Delta^{(0)} + p_0 - p^2/(2M) + i[h^{(0)}]^2 f_0(p_0, \boldsymbol{p})}, \\ f_0(p_0, \boldsymbol{p}) =& -i2\mu \left(\frac{\lambda}{2}\right)^{4-D} \int \frac{d^{D-1}\boldsymbol{q}}{(2\pi)^{D-1}} \frac{1}{q^2 - 2\mu p_0 + \mu p^2/M - i0^+} \\ =& -\frac{i\mu}{2\pi}(\lambda - \sqrt{-2\mu p_0 + \mu p^2/M - i0^+}), \end{aligned} \tag{3.6}$$

with $\lambda \sim Q$, the renormalization scale. We use the power divergence subtraction scheme where divergences in space-time dimensions $D = 4$ and lower are subtracted [50].

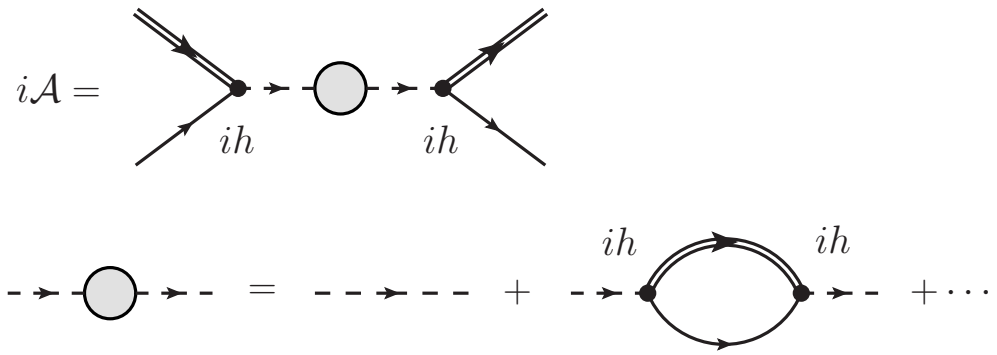


Figure 3.1

Elastic scattering amplitudes $\mathcal{A}^{(\kappa)}$ in $s$- and $p$-waves.

Double line is the $^{14}$C propagator, single line is the neutron propagator, and dashed line is the bare dimer propagator. $\kappa = 0, 1, 2$ corresponds to $^2S_{1/2}$, $^2P_{1/2}$ and $^2P_{3/2}$ channels, respectively.

In Eq. (3.5), the interaction to all orders are iterated to describe a $s$-wave bound state. At low energy, by matching the EFT amplitude Eq. (3.5) to the effective range expansion (ERE)

$$i\mathcal{A}_0(p) = \frac{2\pi}{\mu}\frac{i}{p\cot\delta_0 - ip} \approx \frac{2\pi}{\mu}\frac{i}{-\gamma + \rho(p^2+\gamma^2)/2 - ip}, \tag{3.7}$$

we get

$$\begin{aligned} \frac{2\pi\Delta^{(0)}}{\mu[h^{(0)}]^2} + \lambda =& \gamma - \frac{1}{2}\rho\gamma^2, \\ -\frac{2\pi}{[h^{(0)}]^2\mu^2} =& \rho, \end{aligned} \tag{3.8}$$

where $\mu = M_n M_c/(M_n + M_c)$ is the reduced mass, $\gamma \approx 46.21$ MeV is the $^{15}$C ground state binding momentum, and $\rho$ is the effective range in $s$-wave. There is no experimental constraint on the value of $\rho$, but it has the dimension of length. *A priori* it is not clear if the effective range $\rho$ should scale with the short-distance (high-energy) scale $\rho \sim 1/\Lambda$ or with

the long distance (low-energy) scale $\rho \sim 1/Q$. If it is the former, $\rho$ is a next-to-leading order (NLO) correction whereas if it is the latter, it is a leading order (LO) contribution in EFT.

### 3.2.2 Elastic scattering parameters of $p$-wave

The $p$-wave elastic scattering amplitude is given by a set of diagrams similar to the $s$-wave amplitude, Fig. 3.1. We get

$$i\mathcal{A}_1^\eta(p) = -[h^{(\eta)}]^2 \frac{k^2}{\mu^2} i D_\chi^\eta(\frac{p^2}{2\mu}, 0) = \frac{2\pi}{\mu} \frac{ip^2}{-\frac{2\pi\mu\Delta^{(\eta)}}{[h^{(\eta)}]^2} - \frac{\pi\lambda^3}{2} - \left(\frac{3\lambda}{2} + \frac{\pi}{[h^{(\eta)}]^2}\right) p^2 - ip^3}, \quad (3.9)$$

using the $p$-wave propagator for the $\chi^\eta$ field

$$\begin{aligned} iD_\chi^\eta(p_0, \boldsymbol{p}) =& \frac{i}{\Delta^{(\eta)} - \frac{1}{2\mu}\zeta^2 + \frac{2[h^{(\eta)}]^2}{\mu} f_1(p_0, \boldsymbol{p})}, \\ f_1(p_0, \boldsymbol{p}) =& \frac{1}{4\pi}\left(\zeta^3 - \frac{3}{2}\zeta^2\lambda + \frac{\pi}{2}\lambda^3\right), \end{aligned} \quad (3.10)$$

where $\zeta = \sqrt{-2\mu p_0 + \mu p^2/M - i0^+}$.

As for the $s$-wave, the EFT couplings in $p$-wave can be related to observables by comparing the EFT amplitude Eq. (3.9), and we get for the $p$-wave

$$i\mathcal{A}_1^\eta(p) = i\frac{2\pi}{\mu} \frac{p^2}{p^3 \cot\delta_1^\eta - ip^3} \approx i\frac{2\pi}{\mu} \frac{p^2}{-1/a_1^{(\eta)} + r_1^{(\eta)} p^2/2 - ip^3}, \quad (3.11)$$

and

$$\begin{aligned} -\frac{2\pi\mu\Delta^{(\eta)}}{[h^{(\eta)}]^2} - \frac{\pi}{2}\lambda^3 =& -1/a_1^{(\eta)}, \\ -\frac{3}{2}\lambda - \frac{\pi}{[h^{(\eta)}]^2} =& \frac{1}{2} r_1^{(\eta)}. \end{aligned} \quad (3.12)$$

The ERE parameters $a_1^{(1)}, r_1^{(1)}$ and $a_1^{(2)}, r_1^{(2)}$ can in principle be used to determine the EFT couplings $\Delta^{(1)}, h^{(1)}$ and $\Delta^{(2)}, h^{(2)}$ in the ${}^2P_{1/2}$ and the ${}^2P_{3/2}$ channels, respectively.

However, due to lack of sufficient elastic $n+^{14}$C scattering data, the ERE parameters in $p$-wave are not known. In EFT, it is not clear *a priori* how the couplings should be estimated. In the natural case, where all couplings scale are related to the short-distance scale $\Lambda$, initial $p$-wave interaction would be perturbative. In the presence of shallow bound, virtual or resonance states in $p$-wave, the EFT couplings are fine tuned to scale with powers of the long-distance scale $Q$. Then the $p$-wave operators in Eq. (3.3) need to be treated non-perturbatively [17, 18]. Even in the case where $p$-wave interaction is perturbative, treating it non-perturbatively does not introduce uncontrolled error in the EFT calculation. Thus resumming the $p$-wave interaction with the interactions in Eq. (3.3) to all order gives a result valid in both natural and un-natural cases.

### 3.2.3 $p$-wave resonance

We can determine two out of the four unknown $p$-wave couplings from the known resonance $\frac{1}{2}^-$ state of $^{15}$C using a resonance energy $E_r \approx 1.885$ MeV and resonance width $\Gamma_r \approx 40$ keV in the c.m. frame. This resonance state is in the $^2P_{1/2}$ channel in the EFT. To describe resonance, one needs to treat the $p$-wave interaction non-perturbatively. From the previous chapter, the elastic scattering amplitude near resonance can be written as

$$a_1^{(1)} = -\frac{\mu\Gamma_r}{p_r^5}, \text{ and } r_1^{(1)} = -\frac{2p_r^3}{\mu\Gamma_r}. \tag{3.13}$$

From Eq. 3.13, the couplings $\Delta^{(1)}$ and $h^{(1)}$ can be determined. The $a_1^{(1)}$ and $r_1^{(1)}$ obtained from the $\frac{1}{2}^-$ resonance state when used in the capture cross section Eq. (3.18) give negligible contributions to $^{14}\mathrm{C}(n,\gamma)^{15}\mathrm{C}$ away from the resonance. Near resonance, it produces

a sharp peak. The scaling of the remaining two $p$-wave EFT couplings is determined by analyzing available $^{14}\mathrm{C}(n,\gamma)^{15}\mathrm{C}$ data in the following section.

### 3.3 Capture Cross Section

The $^{14}\mathrm{C}(n,\gamma)^{15}\mathrm{C}$ cross section is calculated in the c.m. frame with core (photon) momentum $\boldsymbol{p}$ ($\boldsymbol{k}$) and $\hat{\boldsymbol{k}}\cdot\hat{\boldsymbol{p}}=\cos\theta$. The incoming momentum $p$ as well as the binding momenta for the ground state $\gamma$ are assumed to be of the order of the low-energy scale, *i.e.*, $p\sim\gamma\sim Q$. The photon at LO has $|\boldsymbol{k}|=k_0\approx(p^2+[\gamma^{(\eta)}]^2)/(2\mu)$ and the Mandelstam variable $s\approx(M_n+M_c)^2=M^2$.

The c.m. differential cross section is

$$\frac{d\sigma}{d\phi d\cos\theta}=\frac{1}{64\pi^2 s}\frac{|\boldsymbol{k}|}{|\boldsymbol{p}|}|\mathcal{M}|^2\approx\frac{1}{64\pi^2M^2}\frac{p^2+[\gamma^{(\eta)}]^2}{2\mu p}|\mathcal{M}|^2, \tag{3.14}$$

where $\gamma\approx 46.21$ MeV.

We only concentrate on the E1 transition. E1 capture to the ground state proceeds though the diagrams in Fig. 3.2. The photon couples to the charge of the $^{14}$C core through minimal coupling. This corresponds to gauging the core momentum $\boldsymbol{p}\to\boldsymbol{p}+Z_c e\boldsymbol{A}$, where $Z_c=6$. The contribution from the first diagram in Fig. 3.2 $(a)$ can be projected onto the capture contribution from initial $^2P_{1/2}$ and $^2P_{3/2}$ channels using the projectors from Eq. (3.4). Including the contribution from diagrams 3.2 $(b)$ and 3.2 $(c)$, that involve the initial state $p$-wave interactions from Eq. (3.3), the amplitude square for the $^2P_{1/2}$ channel is

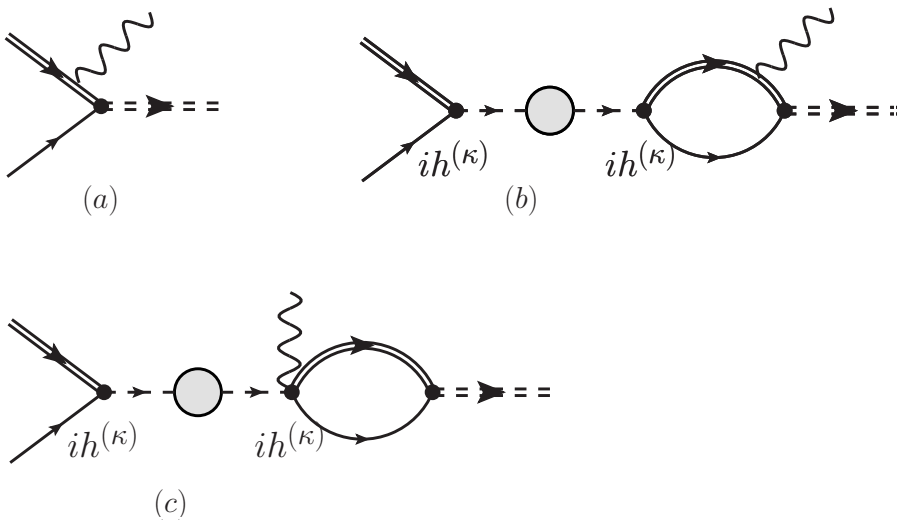


Figure 3.2

E1 capture of $^{14}\mathrm{C}(n,\gamma)^{15}\mathrm{C}$

Double dashed line is the final state $^{15}$C dimer field $\phi$, and the single dashed line is for dressed dimer field $\chi^\eta$ representing initial $p$-wave interaction. Wavy lines represent photons.

$$|\mathcal{M}^{^2P_{1/2}}|^2 = \left|\frac{12eh_0\sqrt{Z_\phi}}{M_c}\right|^2 \frac{32M_nM_cMp^2}{9}\left|g^{^2P_{1/2}}(p)\right|^2 \tag{3.15}$$

$$g^{^2P_{1/2}}(p) = \frac{\mu}{p^2+\gamma^2} + \frac{6\pi\mu}{-1/a_1^{(1)} + r_1^{(1)}p^2/2 - ip^3}\left[\frac{\gamma}{4\pi} + \frac{ip^3-\gamma^3}{6\pi(p^2+\gamma^2)}\right].$$

The first term, without the initial state $p$-wave interaction, in $g^{^2P_{1/2}}$ is from diagram Fig. 3.2 $(a)$. In the $^2P_{3/2}$ channel a similar expression is obtained

$$|\mathcal{M}^{^2P_{3/2}}|^2 = \left|\frac{12eh_0\sqrt{Z_\phi}}{M_c}\right|^2 \frac{16M_nM_cMp^2}{9}\left|g^{^2P_{3/2}}(p)\right|^2 (5-3\cos^2\theta), \tag{3.16}$$

$$g^{^2P_{3/2}}(p) = \frac{\mu}{p^2+\gamma^2} + \frac{6\pi\mu}{-1/a_1^{(2)} + r_1^{(2)}p^2/2 - ip^3}\left[\frac{\gamma}{4\pi} + \frac{ip^3-\gamma^3}{6\pi(p^2+\gamma^2)}\right].$$

The wave function renormalization factor $Z_\phi$ is related to the residue at the pole of the propagator of the $\phi$ particle that represents the $^{15}$C ground state. It is calculated from the dressed $\phi$ propagator as

$$Z_\phi^{-1} = \frac{\partial}{\partial p_0}[D_\phi(p_0, \boldsymbol{p})]^{-1}\Big|_{p_0=p^2/(2M)-B} = 1 + \frac{\mu^2 h_0^2}{2\pi\gamma} = -\frac{1-\rho\gamma}{\rho\gamma}, \tag{3.17}$$

where $B = \gamma^2/(2\mu) \approx 1.218$ MeV is the ground state binding energy.

Then the total cross section is

$$\sigma(p) = \frac{1}{2}\frac{64\pi\alpha}{M_c^2\mu^2}\frac{p\gamma(p^2+\gamma^2)}{1-\rho\gamma}\left[2|g^{^2P_{1/2}}(p)|^2 + 4|g^{^2P_{3/2}}(p)|^2\right], \tag{3.18}$$

where the electron charge is defined as $\alpha = e^2/(4\pi) = 1/137$.

The cross section in Eq. (3.18) depends on three unknown EFT couplings that can be expressed in terms of three ERE parameters: the $s$-wave effective range $\rho$, the $^2P_{3/2}$ channel scattering volume $a_1^{(2)}$, and the $^2P_{3/2}$ channel "effective range" $r_1^{(2)}$. As the ERE parameters are not model-specific definitions, but universal that are in principle directly related to the $n$+$^{14}$C elastic scattering phase shifts, the contributions from Figs. 3.2 $(a)$, $(b)$, and $(c)$ are model-independent. The total $^2P_{1/2}$ and $^2P_{3/2}$ contribution from the tree level diagram Fig. 3.2 $(a)$ without the effective range correction $\rho$ is around $5\mu$b. This is comparable to the data [73, 77] in Fig. 3.4, but also indicates that effective range $\rho$ correction and/or initial state $p$-wave interaction is important at LO to explain the data.

Contributions of diagrams $(a)$, $(b)$, and $(c)$ in Fig. 3.2 depends on the power counting that is used as the order of unknown parameters $a_1^{(2)}$ and $r_1^{(2)}$. The Table 3.1 shows the behavior of the all three diagrams with respect to the given power counting.

Table 3.1

Power counting for E1 capture of $^{14}\mathrm{C}(n,\gamma)^{15}\mathrm{C}$

| $(a_1^{(2)}, r_1^{(2)})$ | Behavior of diagram $(a)$, $(b)$, and $(c)$ |
|---|---|
| $(\sim 1/\Lambda^3, \sim \Lambda)$ (natural case) | $(b)$ and $(c)$ is $Q^3/\Lambda^3$ suppressed compared to $(a)$ |
| $(\sim 1/Q^3, \sim Q)$ (Refs. [17]) | all the three diagrams are of the same order |
| $(\sim 1/(Q^2\Lambda), \sim \Lambda)$ (Refs. [18]) | $(b)$ and $(c)$ is $Q/\Lambda$ suppressed compare to $(a)$ |

In the following section, I will construct a systematic EFT by considering $\rho \sim 1/\Lambda$, $a_1^{(2)} \sim 1/Q^3$, and $r_1^{(2)} \sim Q$. Then, the $s$-wave effective range $\rho$ correction is a NLO effect, and the $^2P_{3/2}$ interactions are LO. I present only the LO result where the effective range $\rho$ contribution is neglected.

## 3.4 Results and Discussion

### 3.4.1 Cross section

The LO cross section in the $^2P_{1/2}$ channel is determined by the $^{15}$C ground state binding momentum $\gamma$, the $\frac{1}{2}^-$ state resonance energy $E_r$, and width $\Gamma_r$.

In Fig. 3.3, we compare the contribution from Fig. 3.2 $(a)$ to those from Fig. 3.2 $(b)$ and $(c)$. The dashed curve shows the non-resonant contribution in the $^2P_{1/2}$ channel and the solid curve shows the $\frac{1}{2}^-$ resonant contribution (in the same $^2P_{1/2}$ channel). As expected, the resonant contribution is large near the resonance energy $E_r \approx 1.885$ MeV, and comparatively negligible elsewhere. More importantly, one notices that the non-resonant contribution is non-negligible throughout the energy region. This implies that interference between the resonant and non-resonant contributions in the total cross section is significant as will be seen later.

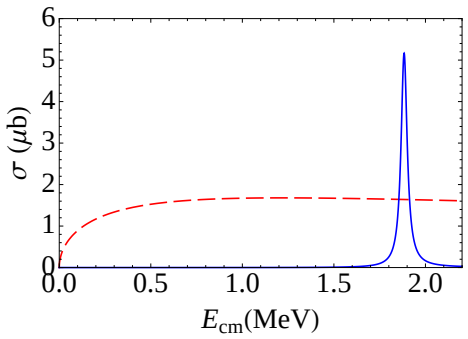


Figure 3.3

Resonant and non-resonant contributions to E1 capture cross section in the $^2P_{1/2}$ channel

Solid (blue) curve is the resonant contribution, and dashed (red) curve is the non-resonant contribution.

In the $^2P_{3/2}$ channel, the undetermined ERE parameters are $a_1^{(2)}$ and$r_1^{(2)}$ at LO. In Fig. 3.4, the total cross section parametrized by $a_1^{(2)} = -n_1/(Q^3)$ and $r_1^{(2)} = 2n_2Q$ is plotted for some reasonable values of $n_1$ and $n_2$ of $\mathcal{O}(1)$. $Q = 40$ MeV is picked. For example, $(n_1, n_2) =$ (2, 1.5) and $(n_1, n_2) =$ (1.5, 1.2) reproduces direct capture data from Ref. [73]. We also show Coulomb dissociation data from Ref. [77]. A $\chi$-square fit to the Coulomb dissociation data with $Q = 40$ MeV gives $(n_1, n_2) =$ (0.818, 1.12). The resonance contribution near $E_{\rm cm} \approx 1.89$ MeV differs from a simple Breit-Wigner form. This is a result of the significant interference between the non-resonant and resonant contributions in the $^2P_{1/2}$ channel alluded to earlier in discussing Fig. 3.3.

### 3.4.2 S-factor

The astrophysical S-factor determines the reaction cross section. Here we present the cross section $\sigma$ in Eq. 3.18 in terms of the $S$-factor, $S_n = \sigma/\sqrt{E_{\rm cm}}$, to use in astrophysical

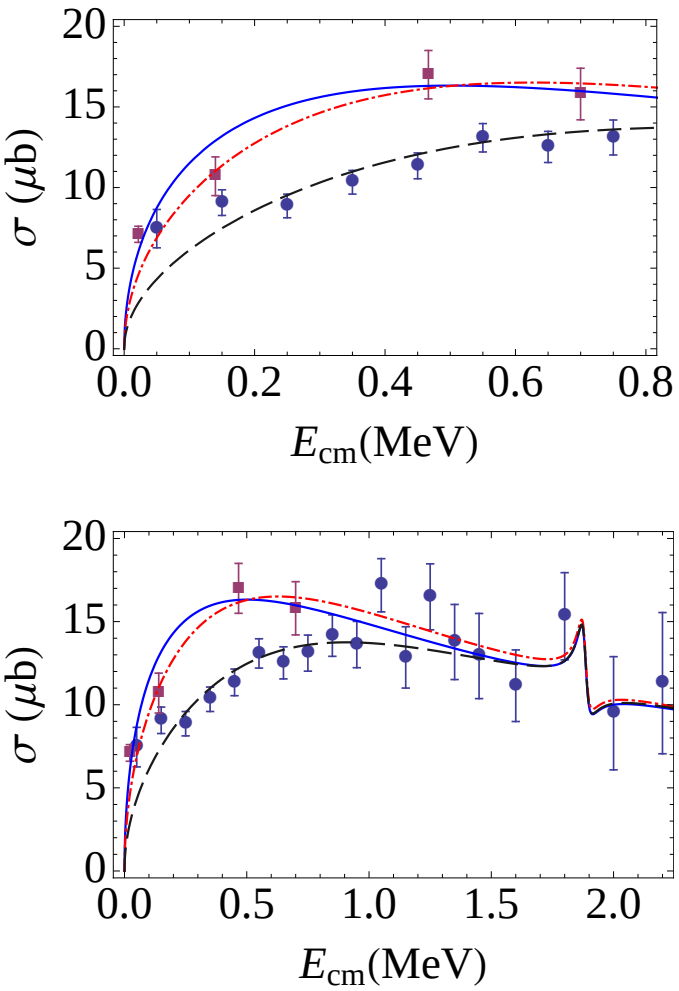


Figure 3.4

E1 capture cross section of $^{14}\mathrm{C}(n,\gamma)^{15}\mathrm{C}$

$\sigma(E_{\mathrm{cm}})$ with $a_1^{(2)} = -n_1/(Q^3)$, $r_1^{(2)} = 2n_2Q$, and $Q = 40$ MeV. Double line is the $^{14}$C propagator, single line the neutron propagator. Solid (blue) curve uses $(n_1, n_2) = (2, 1.5)$; dot-dashed (red) curve uses $(n_1, n_2) = (1.5, 1.2)$; dashed (black) curve uses $(n_1, n_2) = (0.818, 1.12)$. Square (maroon) direct capture data from Ref. [73], circle (dark blue) Coulomb dissociation data from Ref. [77].

calculations at low-energy [84]. As the capture proceeds through $p$-wave initial states to $s$-wave final state, the $S$-factor is a constant at low-energy [84, 69].

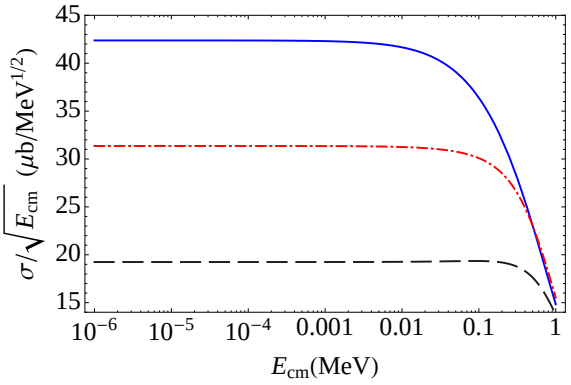


Figure 3.5

E1 capture $S$-factor of $^{14}\mathrm{C}(n,\gamma)^{15}\mathrm{C}$

Ihe same set of parameters (including $\rho = 0$) and legends are used as in Fig. 3.4

In Fig. 3.5 we plot the $S$-factor $S_n = \sigma/\sqrt{E_{\rm cm}}$ using the cross section $\sigma$ from Eq. (3.18). We use the same values of parameters (including $\rho = 0$) used in Fig. 3.4. The three set of values for $S_n$ at low energy are consistent within the $30\%$ accuracy expected of the LO result. Note that the larger values of $S_n$ (solid curve) are close to the values obtained in the microscopic calculation in Ref. [82], and the intermediate values of $S_n$ (dot-dashed curve) are close to the values obtained in the potential model calculation in Ref. [69]. The $S$-factor is a constant at low energy and by expanding it to the lowest order in energy, one get

$$S_n = \frac{16\pi\alpha\sqrt{2\mu}}{M_c^2\gamma(1-\rho\gamma)}\left[12 - 4(a_1^{(1)} + 2a_1^{(2)})\gamma^3 + ([a_1^{(1)}]^2 + 2[a_1^{(2)}]^2)\gamma^6\right] + \mathcal{O}(E_{\rm cm}). \quad (3.19)$$

The contribution from $p$-wave interaction in the ${}^2P_{1/2}$ channel through $a_1^{(1)}$ is negligible at low energy in Fig. 3.3. The result in Eq. (3.19) is accurate to NLO at low energy where contributions from $p$-wave ERE parameters, such as $r_1^{(1)}$ and $r_1^{(2)}$ are, suppressed. The NLO correction to $S_n$ at low energy is through the effective range $\rho$ contribution as seen in Eq. (3.19).

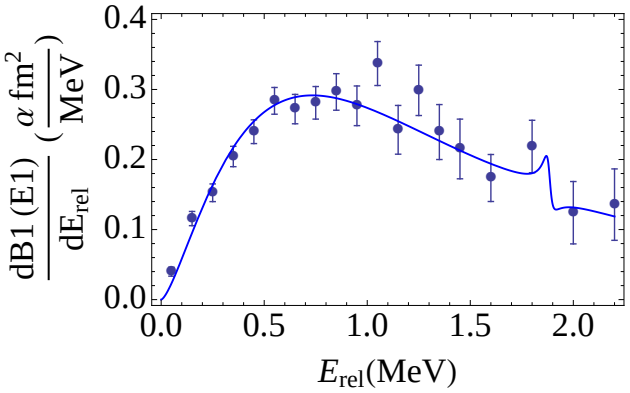


Figure 3.6

E1 reduced transition probability strength of ${}^{14}\mathrm{C}(n,\gamma){}^{15}\mathrm{C}$ .

Solid (blue) curve uses $a_1^{(2)} = -0.818/Q^3$, $r_1^{(2)} = 1.12 \times 2Q$ with $Q = 40$ MeV. Circle (dark blue) data from Ref. [77]

In Fig. 3.6, we look at the E1 reduced transition probability strength [78, 85]

$$\frac{dB(E1)}{dE_{\rm rel}} = \frac{9}{16\pi^3}\frac{\mu E_{\rm cm}}{E_\gamma^3}\sigma(E_{\rm cm}), \tag{3.20}$$

and compared it with available data [77]. We ignored any recoil and equated $E_\gamma = E_{\rm rel}+B$. We used $(n_1 = 0.818, n_2 = 1.12)$ with $Q = 40$ MeV. The agreement with data is not surprising since the capture cross section in Fig. 3.4 was extracted using Eq. (3.20). This

assumed negligible nuclear contribution from the Pb target at the forward angles (large impact parameter) in Ref. [77].

### 3.5 Summary

In this work halo EFT is used to study the radiative capture cross section for $^{14}\mathrm{C}(n,\gamma)^{15}\mathrm{C}$. The dominant contribution to the E1 transition between the initial $p$-wave continuum state and the final $s$-wave ground state of $^{15}$C is calculated. Both resonant and non-resonant interactions are considered. The low neutron separation energy in $^{15}$C nuclei helps to use the single-particle approximation to construct the EFT method. A consistent power counting is developed where the leading contribution involves initial state $p$-wave interactions. The EFT result is written in a model-independent form using ERE parameters. In particular, the result depends on the $^{15}$C ground state binding momentum $\gamma$ and on the scattering parameters $a_1^{(1)}$, $r_1^{(1)}$ , $a_1^{(2)}$, and $r_1^{(2)}$ that encapsulate the interactions in the initial $^2P_{1/2}$ and $^2P_{3/2}$ channels, respectively. The $^2P_{1/2}$ parameters are constrained using the resonance energy and width of the $\frac{1}{2}^-$ resonance state of $^{15}$C. The scattering parameters in the $^2P_{3/2}$ channel are estimated from direct capture and Coulomb dissociation data.

The EFT calculation is shown to be able to describe the energy dependence of the capture cross section at the order of the calculation. The EFT couplings constrained from direct capture reaction and Coulomb dissociation have values consistent with the EFT power counting. The values of the $p$-wave couplings constrained from the direct capture and Coulomb dissociation data are also consistent with each other within the expected EFT error $\mathcal{O}(Q/\Lambda) \sim 30\%$ on the coupling. The contribution from the resonance in the $^2P_{1/2}$

channel differs from a simple Breit-Wigner form due to significant interference with the non-resonant contribution in this channel. It would be interesting to see if this can be confirmed experimentally with more accurate measurements near the resonance energy. Future work should address contributions from the excited $\frac{5}{2}^+$ state of $^{15}$C to the direct capture reaction $^{14}\mathrm{C}(n,\gamma)^{15}\mathrm{C}$. Higher order contributions from two-body currents should be explored as well.

# CHAPTER 4

# ELECTROMAGNETIC FORM FACTORS OF CARBON-15

In the previous chapter, the radiative capture of a neutron on carbon-14 was calculated using EFT. My purpose here is to make sure that EFT can reproduce some known electromagnetic moments and charge radii of spin $\frac{1}{2}^+$ halos . In this work, the electromagnetic form factors for several halo systems that were recently considered are calculated by using EFT.

The single neutron $\frac{1}{2}^+$ halo nuclei ground states of $^{11}$Be, $^{15}$C and $^{19}$C were studied in Refs [24, 23, 86, 87]. The construction of the EFT for these systems is similar though the power counting that determines the relative sizes of the quantum operators is system specific. The $^{15}$C nucleus, spin $\frac{1}{2}^+$, is represented as a shallow bound state of a neutron and a $^{14}$C core in relative $s$-wave. The leading contribution to the capture reaction comes from the E1 transition where the initial state interactions in the ${}^2P_{1/2}$ and ${}^2P_{3/2}$ channels are dominant. The EFT calculations describe the capture and Coulomb dissociation date accurately. A possible contribution from a $\frac{1}{2}^-$ resonance state in the ${}^2P_{1/2}$ state is predicted. The Coulomb dissociation $^{19}\mathrm{C}(\gamma, n)^{18}\mathrm{C}$ was recently calculated by EFT [87]. $^{19}$C is the heaviest known single neutron halo. The Coulomb breakup of $^{19}$C involves an E1 transition and involves the same channels as $^{15}$C. However, here the $p$-wave interactions in the ${}^2P_{1/2}$ and ${}^2P_{3/2}$ channels are shown to be subleading. Finally, the ground state of $^{11}$Be

is considered. This was considered earlier in Refs. [24, 23] where the electric form factor was calculated. The discussion is completed by including the magnetic form factor.

Experiments on elastic electron scattering from a nucleus provide essential information about the internal structure of the nucleus, such as charge density, size of the nuclei, and magnetic properties. Nuclear form factors can be obtained from the experimental results, and theoretical analysis is required to determine internal properties from the form factor. One can determine the nuclear form factor as a ratio of the electron scattering cross section to the cross section for a point like particle as a function of momentum transfer $q$. The $^{15}$C nucleus can be analyzed similarly to electron scattering from a proton target as both involves spin $\frac{1}{2}^+$hadrons.

This chapter is organized as follows. In Section 4.1, the general formalism for the electric and magnetic form factors is introduced. Section 4.2 introduces the EFT interactions and the form factor calculation. Then I discuss the results for the specific halo systems in Section 4.3. The power counting in the three halo systems is considered and discussed. The EFT parameters are chosen correspondingly. Conclusions are presented in Section 4.4.

## 4.1 Formalism

Elastic electron scattering on the $\frac{1}{2}^+$ state os the halo nucleus can be analyzed similarly to electron scattering on a proton target as both involves spin $\frac{1}{2}$ hadrons. The elastic scattering amplitude separates into leptonic and hadronic currents as

$$i\mathcal{M} = [ie\bar{\psi}_e(-\boldsymbol{p}', s')\gamma^\mu\psi_e(-\boldsymbol{p}, s)]\left(-i\frac{g_{\mu\nu}}{q^2}\right)[i\bar{\psi}_\phi(\boldsymbol{p}, a)J^\nu_\phi\psi_\phi(\boldsymbol{p}', a')], \tag{4.1}$$

where $\psi_e(\boldsymbol{p}, s)$ and $\psi_\phi(\boldsymbol{p}, s)$ are the electron and halo nucleus Dirac fields with momenta $\boldsymbol{p}$ and spins $s$, respectively. The photon momentum, $q = p' - p$. Summing over final spins and averaging over initial spins, we obtain

$$\frac{1}{2}\frac{1}{2}\sum_{s,s'}\sum_{a,a'}|\mathcal{M}|^2 \equiv \frac{e^2}{(q^2)^2}g_{\mu\nu}g_{\alpha\beta}L^{\mu\alpha}T^{\nu\beta}, \tag{4.2}$$

where the leptonic contribution is written as

The hadronic contribution is

$$T^{\nu\beta} = \frac{1}{2}\sum_{a,a'}[\bar{\psi}_\phi(\boldsymbol{p}, a)J^\nu\psi_\phi(\boldsymbol{p}', a')][\bar{\psi}_\phi(\boldsymbol{p}', a')J^\beta\psi_\phi(-\boldsymbol{p}, a)] \tag{4.3}$$

Current conservation $q_\mu T^{\mu\nu} = 0 = q_\nu T^{\mu\nu}$ and Lorentz invariance restricts the form of the hadronic current to a generic form

$$\begin{aligned} i\Gamma^\mu =& i\bar{\psi}_\phi(\boldsymbol{p}, a)J^\mu_\phi\psi_\phi(\boldsymbol{p}', a') \\ =& ieZ_c\bar{\psi}_\phi(\boldsymbol{p}, a)\left[\gamma^\mu\mathcal{F}_1(-q^2) + i\frac{\kappa}{2M}\mathcal{F}_2(-q^2)\sigma^{\mu\nu}q_\nu\right]\psi_\phi(\boldsymbol{p}', a') \\ =& ieZ_c\bar{\psi}_\phi(\boldsymbol{p}, a)\left[\frac{p^\mu + p'^\mu}{2M}\mathcal{F}_1(-q^2) + i\frac{\mathcal{F}_1(-q^2) + \kappa\mathcal{F}_2(-q^2)}{2M}\sigma^{\mu\nu}q_\nu\right]\psi_\phi(\boldsymbol{p}', a'), \end{aligned} \tag{4.4}$$

using the Gordon identity. The constant $\kappa$ is the anomalous magnetic moment and $Z_c$ is the charge of the halo nucleus core. For non-relativistic kinematics in the Breit frame $(q_0 = 0, \boldsymbol{q})$, we get

$$i\Gamma^0 = ieZ_c\bar{u}_\phi(\boldsymbol{p}, a)\mathcal{F}_1(|\boldsymbol{q}|^2)u_\phi(\boldsymbol{p}', a'), \tag{4.5}$$

$$i\Gamma^i = ieZ_c\bar{u}_\phi(\boldsymbol{p}, a)\left[\frac{p^i + p'^i}{2M}\mathcal{F}_1(|\boldsymbol{q}|^2) + i\frac{\mathcal{F}_1(|\boldsymbol{q}|^2) + \kappa\mathcal{F}_2(|\boldsymbol{q}|^2)}{2M}\epsilon^{ijk}\sigma_k q_j\right]u_\phi(\boldsymbol{p}', a') \tag{4.6}$$

In the Sach form, the charge $G_E(|\boldsymbol{q}|^2)$ and magnetic $G_M(|\boldsymbol{q}|^2)$ form factors can be written as

$$\begin{aligned} G_E(|\boldsymbol{q}|^2) =& \mathcal{F}_1(|\boldsymbol{q}|^2) - \frac{|\boldsymbol{q}|^2}{4M^2}\kappa\mathcal{F}_2(|\boldsymbol{q}|^2), \\ G_M(|\boldsymbol{q}|^2) =& \mathcal{F}_1(|\boldsymbol{q}|^2) + \kappa\mathcal{F}_2(|\boldsymbol{q}|^2). \end{aligned} \tag{4.7}$$

In EFT, the form factors $\mathcal{F}_i$s are $\mathcal{O}(1)$ in the $Q/\Lambda$ expansion as we show later in Section 4.2. We count $q \sim Q$ at low photon exchange momentum. Thus the magnetic form factor $G_M$ gets contribution from both $\mathcal{F}_1$ and $\mathcal{F}_2$ whereas the electric form factor $G_E$ only gets contribution from $\mathcal{F}_1$ upto NLO. The $\mathcal{F}_2$ term in $G_E$ is the so called Darwin-Foldy contribution. At the same order, there is also a contribution from the relativistic motion associated with the "zitterbewegung" matter radius.

The electric and magnetic form factors are normalized, such that for small $|\boldsymbol{q}|$

$$G_E(|\boldsymbol{q}|^2) \approx 1 - \frac{1}{6}\langle r_E^2\rangle|\boldsymbol{q}|^2 + \cdots, \tag{4.8}$$

where $\sqrt{\langle r_E^2\rangle}$ is the charge radius and

$$\frac{eZ_c}{2M}G_M(|\boldsymbol{q}|^2) \approx \kappa_\phi\mu_N\left[1 - \frac{1}{6}\langle r_M^2\rangle|\boldsymbol{q}|^2 + \cdots\right], \tag{4.9}$$

where $\kappa_\phi$ is the halo nucleus magnetic moment and $\sqrt{\langle r_M^2\rangle}$ the magnetic radius.

## 4.2 Effective Field Theory

### 4.2.1 Elastic scattering in $s$-wave

The halo nuclei $^{11}$Be, $^{15}$C and $^{19}$C ground states all have spin-parity assignment $\frac{1}{2}^+$. They are treated as a shallow bound state of a single neutron and a spin zero core in the $s$-wave. This is reasonable as the binding energy of the ground state is much smaller than the

energy needed to break the core or the excited state energies of the core [24, 23, 86, 87]. The EFT calculations of these halo systems, so far, agree with available data within the estimated theoretical errors.

In Chapter 3, I described the elastic scattering parameters for $^{14}\mathrm{C}(n,\gamma)^{15}\mathrm{C}$. For completeness here, I rewrite Eq. 3.8 by setting $h^{(0)} = h$ and $\Delta^{(0)} = \Delta$ as

$$\begin{aligned} \frac{2\pi\Delta^{(0)}}{\mu[h]^2} + \lambda =& \gamma - \frac{1}{2}\rho\gamma^2, \\ -\frac{2\pi}{[h]^2\mu^2} =& \rho, \end{aligned} \tag{4.10}$$

where $\mu = M_n M_c/(M_n + M_c)$ is the reduced mass, $\gamma \approx 46.21$ MeV is the $^{15}$C ground state binding momentum, and $\rho$ is the effective range in $s$-wave.

The binding momentum $\gamma$ is determined from the binding energy $B = \gamma^2/(2\mu)$. The effective range $\rho$ is typically less constrained from data as the elastic neutron scattering data are hard to find. However, $\rho$ can be constrained from radiative capture or Coulomb dissociation data when available. In EFT power counting, $\gamma \sim Q$ for shallow bound states and contributes at leading order. *A priori* it is not known how $\rho$ (that has dimensions of length) should scale. If $\rho \sim 1/\Lambda$, it is a next-to-leading order effect whereas if $\rho \sim 1/Q$, it contributes at leading order. In the halo systems I consider later in Section 4.3, $\rho \sim 1/\Lambda$.

### 4.2.2 Electromagnetic form factors from EFT

The form factor calculations also depend on the magnetic moment coupling of the neutron and possible two-body currents. The two-body current contribution is subleading

that will be shown later. For completeness, the following operators are consideredd in addition to the interactions in Eq. (2.4)

$$O_{EM} = 2\kappa_n \mu_N N^\dagger (\frac{\boldsymbol{\sigma}}{2} \cdot \boldsymbol{B}) N + \mu_N L_M \phi^\dagger (\boldsymbol{\sigma} \cdot \boldsymbol{B}) \phi,$$

where $\kappa_N = -1.91304$ is the neutron anomalous magnetic moment, $\mu_N$ is the nuclear magneton. $L_M$ is the couplings for a magnetic two-body current.

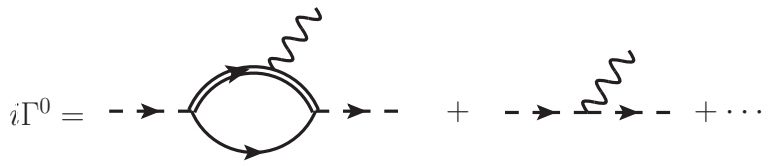


Figure 4.1

EFT calculation of $\Gamma^0$

The wavy lines correspond to $A_0$ photons, and single dash lines corresponding to group state of $\frac{1}{2}^+$ halo nucleus

The EFT calculation of $\Gamma^0$ corresponding to the diagram in Fig. 4.1. We get

$$i\Gamma^0 = ieZ_c Z_\phi \bar{u}_\phi(\boldsymbol{p}, a) \left[ h^2 \frac{\mu M_c}{\pi |\boldsymbol{q}|} \tan^{-1} \left( \frac{\mu |\boldsymbol{q}|}{2 M_c \gamma} \right) + 1 \right] u_\phi(\boldsymbol{p}', b) \tag{4.11}$$

where the first term is the contribution from the one-loop diagram and the second term is from the tree-level diagram. The overall factor $Z_\phi$ is the wavefunction renormalization that is defined as the residue of the dimer $\phi$ propagator at the bound state energy pole

$$Z_\phi^{-1} = \frac{\partial}{\partial p_0} [D_\phi(p_0, \boldsymbol{p})]^{-1} \Big|_{p_0 = p^2/(2M) - B} = 1 + \frac{\mu^2 h^2}{2\pi\gamma} = -\frac{1 - \rho\gamma}{\rho\gamma}. \tag{4.12}$$

The relation $B = \gamma^2/(2\mu)$ is used for the shallow bound nucleus and from Eq. 4.10, $h^2 = -2\pi/(\rho\mu^2)$. For the halo nuclei we consider, $\rho \sim 1/\Lambda$ and it is seen that the second

term in Eq. (4.11) is $\mathcal{O}(Q/\Lambda)$ smaller compared to the first term and constitutes the NLO correction.

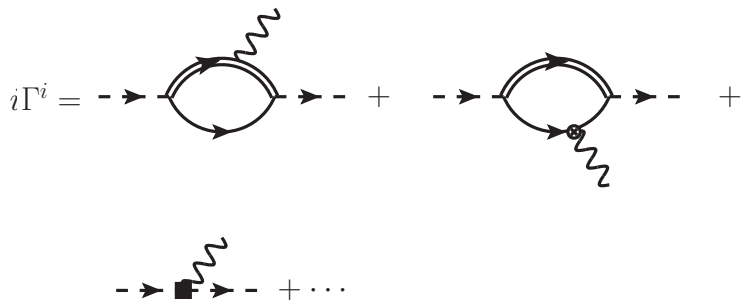

Figure 4.2

EFT calculation of $\Gamma^i$

The wavy lines correspond to $A_i$ photons, and single dash lines corresponding to group state of $\frac{1}{2}^+$ halo nucleus

The EFT calculation of $\Gamma^i$ corresponding to the diagrams in Fig. 4.2 gives

$$\begin{aligned} i\Gamma^i =& ieZ_cZ_\phi\bar{u}_\phi(\boldsymbol{p},a)\left\{\frac{p_i+p_i'}{2M}\left[h^2\frac{\mu M_c}{\pi|\boldsymbol{q}|}\tan^{-1}\left(\frac{\mu|\boldsymbol{q}|}{2M_c\gamma}\right)+1\right]\right. \\ &\left.+i\frac{\mu_N}{eZ_c}\left[h^2\kappa_n\frac{\mu M_n}{\pi|\boldsymbol{q}|}\tan^{-1}\left(\frac{\mu|\boldsymbol{q}|}{2M_n\gamma}\right)+L_M\right]\epsilon^{ijk}\sigma_j q_k\right\}u_\phi(\boldsymbol{p}',a'). \end{aligned} \tag{4.13}$$

$\Gamma^i$ has a contribution from magnetic photons that includes a contribution from the electromagnetic current generated by the orbital motion of the charged $^{10}$Be, $^{14}$C or $^{18}$C core. The two-body current coupling $L_M$ is dimensionless, and we will count it as $\mathcal{O}(1)$ in the $Q/\Lambda$ expansion. Thus, it is seen that this contribution is NLO in Eq. (4.13).

Comparing Eq.4.13 and Eq. 4.11 with Eq. 4.5 and Eq.4.6, respectively, we get expressions for the electric form factors in the Sach form

$$\begin{aligned} G_E(|\boldsymbol{q}|^2) =& Z_\phi \left[ h^2 \frac{\mu M_c}{\pi |\boldsymbol{q}|} \tan^{-1}\left( \frac{\mu |\boldsymbol{q}|}{2 M_c \gamma} \right) + 1 \right] \\ \approx& 1 - \frac{\mu^2}{12 M_c^2 \gamma^2} \frac{1}{1-\rho\gamma} |\boldsymbol{q}|^2 + \cdots , \end{aligned} \tag{4.14}$$

expanding in small momenta $|\boldsymbol{q}|$. In the electric form factor we ignored the Darwin-Foldy contributions. In the EFT the core of the halo nucleus is treated as point-like. However, to compare the charge radius with experimental values, one has to add the finite charge radius of the core in quadrature. Then the electric charge radius

$$\begin{aligned} \langle r_E^2 \rangle &= \frac{\mu^2}{2 M_c^2 \gamma^2} \frac{1}{1-\rho\gamma} + \langle r_c^2 \rangle, \\ \langle r_E^2 \rangle - \langle r_c^2 \rangle &\approx \frac{\mu^2}{2 M_c^2 \gamma^2} (1 + \rho\gamma) \end{aligned} \tag{4.15}$$

expanded to NLO where $\sqrt{\langle r_c^2 \rangle}$ is the core charge radius. The LO charge radius is entirely determined by the halo nucleus binding energy.

In the Sach form we have for the magnetic form factor

$$\begin{aligned} \frac{e Z_c}{2M} G_M(|\boldsymbol{q}|^2) =& \mu_N Z_\phi \left[ \frac{h^2 g_n}{2} \frac{\mu M_n}{\pi |\boldsymbol{q}|} \tan^{-1}\left( \frac{\mu |\boldsymbol{q}|}{2 M_n \gamma} \right) + L_M \right] \\ \approx& (\kappa_n - L_M \rho\gamma) \mu_N \frac{1}{1-\rho\gamma} - \kappa_n \mu_N \frac{\mu^2}{12 M_n^2 \gamma^2} \frac{q^2}{1-\rho\gamma}, \end{aligned} \tag{4.16}$$

expanding around $\boldsymbol{q} = 0$ which gives the magnetic moment of the halo nucleus as

$$\kappa_\phi = (\kappa_n - L_M \rho\gamma) \frac{1}{1-\rho\gamma} \approx k_n + (\kappa_n - L_M) \gamma\rho, \tag{4.17}$$

to NLO.

## 4.3 Results

Here I discuss the results for the electric and magnetic form factors. Up to NLO, the EFT result for the charge radius $\sqrt{\langle r_E^2 \rangle}$ depends only on the binding momentum $\gamma$ and the effective range $\rho$ in $s$-wave. In the magnetic moment calculation, we recover the Schmidt values at LO which is just the neutron magnetic moment in this case. At NLO, we get a contribution from the effective range $\rho$ and the two-body current.

### 4.3.1 $^{15}$C

For $^{15}$C we have the LO result $\kappa_\phi^{(LO)} = \kappa_n = -1.9304$. A shell model calculation provide that $\kappa_\phi$= $-1.813$ [88]. Experimentally only the magnitude of the magnetic moment is known as $\kappa_\phi^{(exp)} = (1.720 \pm 0.009)$ [89]. Assuming a shell-model configuration with a valence $s$-wave neutron dominating the $^{15}$C ground state wave function with 97-98% probability, a tentative experimental value $\kappa_\phi^{(exp)} = -(1.77 \pm 0.05)$ [89] was extracted. This value would correspond to a NLO contribution of about 9% which is smaller than expected, but within the expected $\sim 40\%$ NLO contribution. From Eq. 4.17, the experimental value for $\kappa_\phi$ can be used to constrain the relation between $L_M$ and $\rho$ as

$$L_M = \kappa_n - \frac{\kappa_\phi^{(exp)} - \kappa_n}{\gamma\rho}. \tag{4.18}$$

This constrain helps to estimate the NLO contribution to the magnetic form factor (and the cross section). We vary $\rho \sim 1/\Lambda$ over a range such that the NLO contribution is within $40\%$. This correspond to $\rho \sim -3/m_\pi$ to $1/m_\pi$. The results are plotted in Fig. 4.3.

The values of $\rho$ $-3/m_\pi$ and $1/m_\pi$ give $L_M$ as $-1.8$ and $-2.4$, respectively. These $L_M$values satisfy the power counting mentioned above.

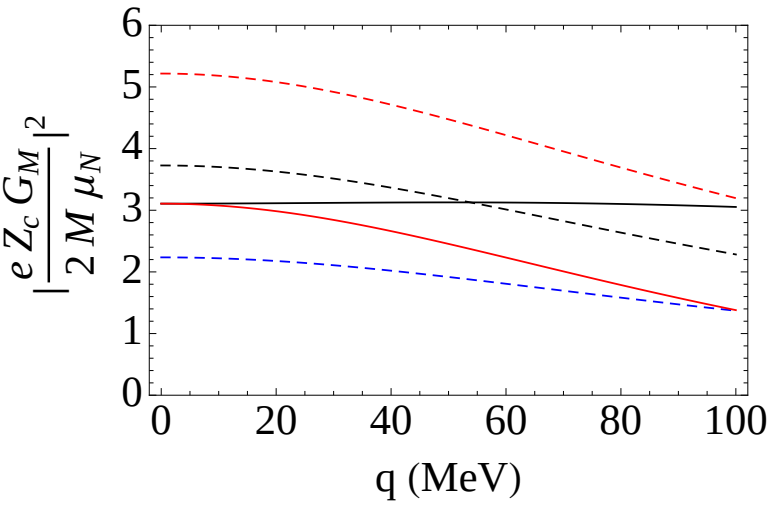


Figure 4.3

$^{15}$C magnetic form factor

Black dashed curve is for LO result, and red and blue dashed curves show the $40\%$ NLO contribution. Black solid curve is for $\rho = -3/m_\pi$ and red solid curve is for $\rho = 1/m_\pi$.

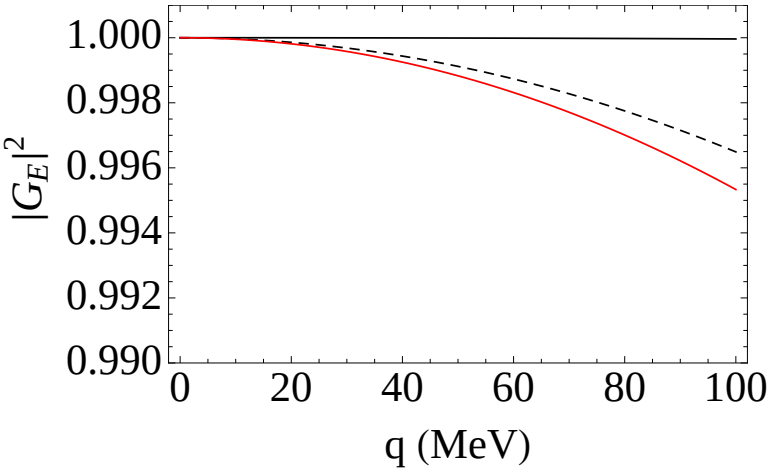


Figure 4.4

$^{15}$C Charge form factor

Black dashed curve is for LO result. Black and red solid curves are for $\rho$ of $-3/m_\pi$ and $1/m_\pi$, respectively in the NLO.

From the EFT result, one can predicts the LO result of $\langle r_E^2 \rangle - \langle r_c^2 \rangle \approx 0.04 fm^2$, and value of $\rho$ is required to estimate the NLO contribution.

### 4.3.2 $^{11}$Be

For $^{11}$Be we have LO result $\kappa_\phi^{(LO)} = \kappa_n = -1.9304$ that disagrees with experimental result $\kappa_\phi^{(exp)} = -1.6814$ [90] by about $14\%$. Fitting the NLO result with $\gamma = 0.15$ fm$^{-1}$ and $\rho = 2.7$ fm [91] to the data gives $L_M = -2.5$, which is reasonable for a dimensionless number. This is similar to the value of $L_M$ we had in the carbon 15 system.

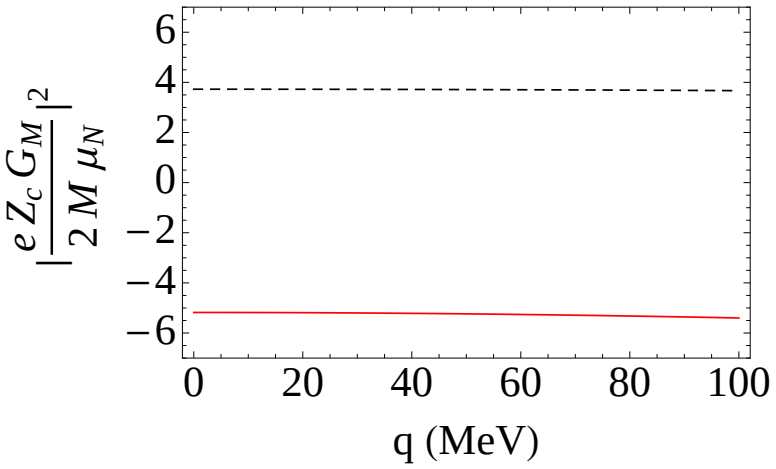


Figure 4.5

$^{11}$Be magnetic form factor

Black dashed curve is for LO result, and red solid curve is for NLO with $\gamma = 0.15$ fm$^{-1}$ and $\rho = 2.7$ fm [91].

The $^{11}$Be experimental charge radii is $\langle r_E^2 \rangle^{\frac{1}{2}} = 2.463$ fm and charge radii of the core, $^{10}$Be, is $\langle r_c^2 \rangle^{\frac{1}{2}} = 2.357$ fm [90]. From our LO result, charge radii of $^{11}$Be is $\approx 2.396$ fm and with NLO result, it is $\approx 2.412$ fm. This value is corresponding to a NLO contribution

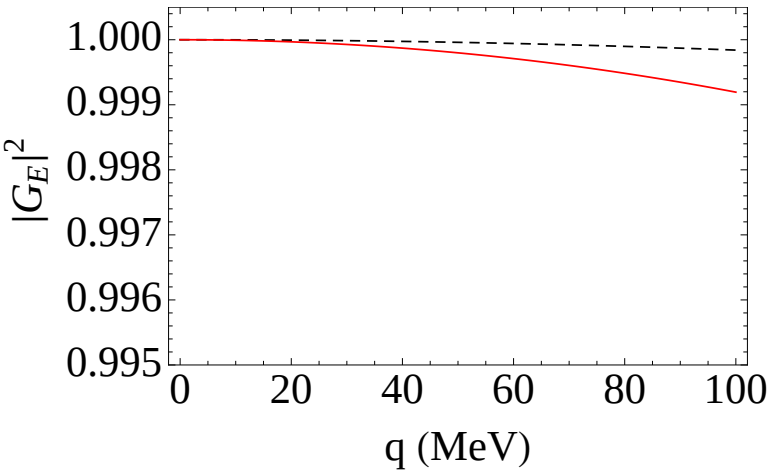


Figure 4.6

$^{11}$Be charge form factor

Black dashed curve is for LO result, and red solid curve is for NLO with $\gamma = 0.15$ fm$^{-1}$ and $\rho = 2.7$ fm [91] .

about $20\%$ is smaller than the expected, but within the expected $\sim 40\%$. This calculation is also done in Ref. [91].

### 4.3.3 $^{19}$C

For $^{19}$C we have LO result $\kappa_\phi^{(LO)} = \kappa_n = -1.9304$. Experimental values are not available for both magnetic moment and electric charge radii of $^{19}$C. Here, a range of values for $\kappa_\phi$ is predicted by changing the value of $L_M$ from $-2$ to 2. According to Eq. 4.18, $\kappa_\phi$ changes linearly with $L_M$ as shown in Fig. 4.7. The previous systems C-15 and Be-11 would suggest perhaps $L_M \sim -2$, which would predict a magnetic moment closer to the Schmidt value.

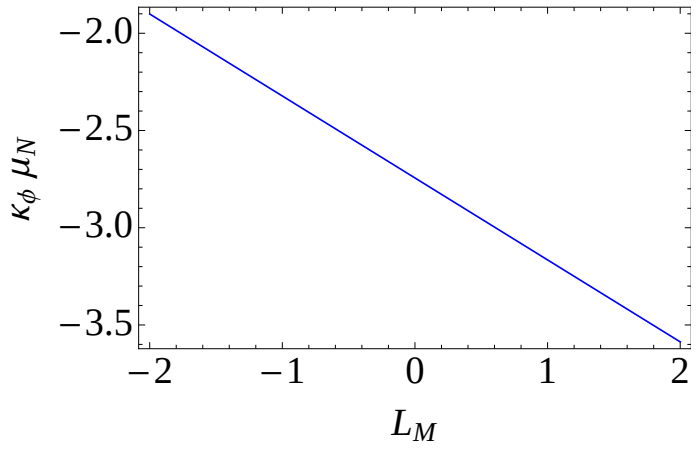


Figure 4.7

$^{19}$C magnetic moment

Here $B = 0.575$ MeV and $\rho = 2.6$ fm [87] are used

Estimated values for $\langle r_E^2 \rangle - \langle r_c^2 \rangle$ are $0.05$ fm$^2$ and $0.075$ fm$^2$ at LO and NLO, respectively.

## 4.4 Summary

In this work, I presented electromagnetic form factors of several halo nuclei. From EFT, we obtained expressions for both magnetic moment and charge radii of a halo nuclei which ground state spin $\frac{1}{2}^+$. Depending on the power counting, the magnetic moments of three halo nuclear systems were predicted or estimated at LO and NLO where two-body currents appear. The EFT result for the charge radii is tested for $^{11}$Be, and the value of the Magnetic moment coupling ($L_M$) is consistent with the EFT power counting. For $^{15}$C and $^{19}$C charge radius is predicted, and $L_M$ is estimated according to the EFT power counting. It is important to have experimental data in order to check the accuracy of the EFT approach.

# CHAPTER 5

# CONCLUSIONS

In this work a model independent calculations for two important halo nuclear reactions are provided by using effective field theory. The halo EFT is constructed in the single-particle approximation, taking advantage of the low neutron separation energy of the halo nuclei. I considered both resonance and non-resonance states and presented the power counting in order to reproduce available experimental results. Further, I used EFT formalism to derive expression for electromagnetic form factor of carbon-15 which also can be used to study both $^{11}$Be and $^{19}$C halo systems.

In the $^{7}\mathrm{Li}(n,\gamma)^{8}\mathrm{Li}$ calculation, previous halo EFT calculation of the $^{7}\mathrm{Li}(n,\gamma)^{8}\mathrm{Li}$ capture reaction is extended by including the complete E1 transition at leading order, as well as the leading M1 capture at low energies. The E1 capture from $s$-waves to the excited state in $^{8}\mathrm{Li}$ that contributes about $10\%$ to the cross section is included explicitly at very low energy. The EFT expression for the capture of $^{7}\mathrm{Li}(n,\gamma)^{8}\mathrm{Li}$ is consistent with very low energy data (below resonance energy). Available capture data near resonance have large errors that affects the quality of the fit. The fact that halo EFT is able to describe resonance scattering (as shown in Section 2.1.2.2), but not to reproduce M1 capture might indicate the limitation of the current approach. However, the apparent discrepancy in the input related to the $3^{+}$ resonance width that is used in the $^{5}P_{3}$ elastic scattering and M1 capture

reaction is unlikely to be resolved with the current experimental information. More precise capture data around where M1 capture dominates is needed to conclusively state if the single-particle approximation is sufficient to describe M1 capture in $^7\mathrm{Li}(n,\gamma)^8\mathrm{Li}$.

As discussed in Section 2.2, the M1 capture could be on the outer edge of the range of applicability. To expand this EFT range, other degrees of freedom have to be incorporated. Within the present two-body treatment, the inclusion of the $\frac{1}{2}^-$ excited state in $^7$Li core is the first step towards this goal. The next, more radical extension is to take the leading configuration of the $^7$Li as a bound state of elementary alpha and triton "cores". In such a three-body approach, not only the ground and the $\frac{1}{2}^-$ excited states in $^7$Li could be considered, but also the $\frac{7}{2}^-$ state which, according to microscopic approaches [33, 34, 29], is important to properly describe the $3^+$ resonance. Nevertheless, the apparent discrepancy in the input related to the $3^+$ resonance width that is used in the $^5P_3$ elastic scattering and M1 capture reaction is unlikely to be resolved with current experimental information. More precise capture data around $0.22$ MeV (where M1 capture dominates) is needed to conclusively state if the single-particle approximation is sufficient to describe M1 capture in $^7\mathrm{Li}(n,\gamma)^8\mathrm{Li}$.

In Chapter 3, I expained the radiative capture cross section for $^{14}\mathrm{C}(n,\gamma)^{15}\mathrm{C}$ in halo EFT. The dominant contribution from the E1 transition between initial $p$-wave continuum state and final $s$-wave ground state of $^{15}$C is calculated. The EFT calculation is shown to be able to describe the energy dependence of the capture cross section at the order of the calculation. The EFT couplings constrained from direct capture reaction and Coulomb dissociation have values consistent with the EFT power counting. The values of the $p$-

wave couplings constrained from the direct capture and Coulomb dissociation data are also consistent with each other within the expected EFT error $\mathcal{O}(Q/\Lambda) \sim 30\%$ on the coupling. Future work should address contributions from the excited $\frac{5}{2}^+$ state of $^{15}$C to the direct capture reaction $^{14}\mathrm{C}(n,\gamma)^{15}\mathrm{C}$.

The electromagnetic form factors of halos are considered in the Chapter 4. The EFT results were tested for three halo nuclei systems $^{11}$Be , $^{15}$C, and $^{19}$C with ground states of $\frac{1}{2}^+$. Based on the available data, magnetic moment and charge radii were predicted or estimated. There are not sufficient data to test the accuracy of the EFT approach.

Other than the above mentioned improvements for both $^{14}\mathrm{C}(n,\gamma)^{15}\mathrm{C}$ and $^{7}\mathrm{Li}(n,\gamma)^{8}\mathrm{Li}$, future studies would involve the calculation of $^{7}\mathrm{Be}(p,\gamma)^{8}\mathrm{B}$ by adding the Coulomb contribution to the EFT results from $^{7}\mathrm{Li}(n,\gamma)^{8}\mathrm{Li}$. Also I am interested in studying electromagnetic form factors of the halo systems with ground state of spin $2$ to further understand the $^{8}$Li halo.

REFERENCES


[1] S. Weinberg. *The Quantum Theory of Fields, Vol.2: Modern Application*. Cambridge University Press,Cambridge,UK., 2001.

[2] R. Machleidt, K. Holinde, and C. Elster. The bonn meson-exchange model for the nucleonnucleon interaction. *Physics Reports*, 149(1):1–89, 1987.

[3] V. G. J. Stoks, R. A. M. Klomp, C. P. F. Terheggen, and J. J. de Swart. Construction of high-quality *NN* potential models. *Phys. Rev. C*, 49:2950–2962, 1994.

[4] R. B. Wiringa, V. G. J. Stoks, and R. Schiavilla. Accurate nucleon-nucleon potential with charge-independence breaking. *Phys. Rev. C*, 51:38–51, 1995.

[5] M. Butler and J.W. Chen. Elastic and inelastic neutrinodeuteron scattering in effective field theory. *Nuclear Physics A*, 675(34):575 – 600, 2000.

[6] C.A. Bertulani and A. Gade. Nuclear Astrophysics with Radioactive Beams. *Phys.Rept.*, 485:195–259, 2010.

[7] T. Rauscher. The Path to Improved Reaction Rates for Astrophysics. *Int.J.Mod.Phys.*, E20:1071–1169, 2011.

[8] J. Al-Khalili. An introduction to halo nuclei. In J. Al-Khalili and E. Roeckl, editors, *The Euroschool Lectures on Physics with Exotic Beams, Vol. I*, volume 651 of *Lecture Notes in Physics*, pages 77–112. Springer Berlin Heidelberg, 2004.

[9] I. Tanihata, H. Hamagaki, O. Hashimoto, S. Nagamiya, Y. Shida, N. Yoshikawa, O. Yamakawa, K. Sugimoto, T. Kobayashi, D.E. Greiner, N. Takahashi, and Y. Nojiri. Measurements of interaction cross sections and radii of He isotopes. *Physics Letters B*, 160(6):380 – 384, 1985.

[10] I. Tanihata, H. Hamagaki, O. Hashimoto, Y. Shida, N. Yoshikawa, K. Sugimoto, O. Yamakawa, T. Kobayashi, and N. Takahashi. Measurements of interaction cross sections and nuclear radii in the light $p$-shell region. *Phys. Rev. Lett.*, 55:2676–2679, 1985.

[11] P.G. Hansen and B Jonson. The neutron halo of extremely neutron-rich nuclei. *Europhysics Letters*, 4:409–414, 1987.

[12] M. Wiescher, J Gorres, and H. Schatz. Break-out reactions from the CNO cyclese. *J. Phys. G: Nucl. Part. Phys.*, 25:R133, 1999.

[13] P. Navrtil, C.A. Bertulani, and E. Caurier. $^{7}\mathrm{Be}(p,\gamma)^{8}\mathrm{B}$ S-factor from *ab initio* wave functions. *Physics Letters B*, 634(23):191 – 194, 2006.

[14] P. Navrátil, C. A. Bertulani, and E. Caurier. $^{7}\mathrm{Be}(p,\gamma)^{8}\mathrm{B}$ Sfactor from *ab initio* no-core shell model wave functions. *Phys. Rev. C*, 73:065801, 2006.

[15] E. Nielsen, D.V. Fedorov, A.S. Jensen, and E. Garrido. The three-body problem with short-range interactions. *Physics Reports*, 347(5):373 – 459, 2001.

[16] R.J. Glauber. *Lectures in Theoretical Physics*. Wiley(Interscience), 1959.

[17] C. A. Bertulani, H. W. Hammer, and U. Van Kolck. Effective Field Theory for Halo Nuclei. *Nucl. Phys.*, A712:37–58, 2002.

[18] P. F. Bedaque, H. W. Hammer, and U. van Kolck. Narrow resonances in effective field theory. *Phys. Lett.*, B569:159–167, 2003.

[19] R. Higa, H.-W. Hammer, and U. van Kolck. Alpha Alpha Scattering in Halo Effective Field Theory. *Nucl.Phys.*, A809:171–188, 2008.

[20] B. A. Gelman. Narrow resonances and short-range interactions. *Phys.Rev.*, C80:034005, 2009.

[21] D. L. Canham and H.-W. Hammer. Universal properties and structure of halo nuclei. *Eur. Phys. J. A*, 37:367–380, 2008.

[22] D. L. Canham and H.-W. Hammer. Range corrections for two-neutron halo nuclei in effective theory. *Nucl. Phys. A*, 836:275–292, 2010.

[23] H.-W. Hammer and D.R. Phillips. Electric properties of the Beryllium-11 system in Halo EFT. *Nucl. Phys. A*, 865:17–42, 2011.

[24] D. R. Phillips and H. W. Hammer. Electromagnetic properties of the Be-11 nucleus in halo EFT. *EPJ Web Conf.*, 3:06002, 2010.

[25] V. Lensky and M. C. Birse. Coupled-channel effective field theory and proton-$^{7}$Li scattering. *Eur. Phys. J. A*, 47:142, 2011.

[26] L. H. Kawano, W. A. Fowler, R. W. Kavanagh, and R. A. Malaney. Signatures of inhomogeneity in the early universe. *Astrophys. J.*, 372:1–7, 1991.

[27] E. G. Adelberger, S. M. Austin, J. N. Bahcall, A. B. Balantekin, G. Bogaert, L. S. Brown, L. Buchmann, F. E. Cecil, A. E. Champagne, L. de Braeckeleer, C. A. Duba, S. R. Elliott, S. J. Freedman, M. Gai, G. Goldring, C.R. Gould, A. Gruzinov, W. C. Haxton, K.M. Heeger, C. W. Henley, E.and Johnson, M. Kamionkowski, R. W. Kavanagh, S. E. Koonin, K. Kubodera, K. Langanke, T. Motobayashi, V. Pandharipande, P. Parker, R. G. H. Robertson, C. Rolfs, R. F. Sawyer, N. Shaviv, T. D. Shoppa, K. A. Snover, E. Swanson, R.E. Tribble, S. Turck-Chièze, and J. F. Wilkerson. Solar fusion cross sections. *Rev. Mod. Phys.*, 70:1265–1291, 1998.

[28] B. Davids and S. Typel. Electromagnetic dissociation of $^8B$ and the astrophysical S -factor for $^7\mathrm{Be}(p,\gamma)^8\mathrm{B}$. *Phys. Rev. C*, 68(4):045802, 2003.

[29] P. Descouvemont. Reanalysis of the $^7\mathrm{Be}(p,\gamma)^8\mathrm{B}$ S factor in a microscopic model. *Phys. Rev. C*, 70:065802, 2004.

[30] C.A. Bertulani. $^7\mathrm{Be}(p,\gamma)^8\mathrm{B}$ cross section from indirect breakup experiments. *Zeitschrift fr Physik A Hadrons and Nuclei*, 356:293, 1996.

[31] P. Navratil, C.A. Bertulani, and E. Caurier. $^7\mathrm{Be}(p,\gamma)^8$B S-factor from *ab initio* wave functions. *Phys.Lett.*, B634:191–194, 2006.

[32] P. Navratil, C.A. Bertulani, and E. Caurier. $^7\mathrm{Be}(p,\gamma)^8$B S-factor from *ab initio* no-core shell model wave functions. *Phys.Rev.*, C73:065801, 2006.

[33] Navratil, P. and Roth, R. and Quaglioni, S. Ab initio many-body calculations of nucleon scattering on $^4He$,$^7$ $Li$,$^7$ $Be$,$^{12}$ $C$ and $^{16}$O. *Phys.Rev.*, C82:034609, 2010.

[34] K. Bennaceur, F. Nowacki, J. Okolowicz, and M. Ploszajczak. Study of the $^7\mathrm{Be}(p,\gamma)^8\mathrm{B}$ and $^7\mathrm{Li}(n,\gamma)^8\mathrm{Li}$ capture reactions using the shell model embedded in the continuum. *Nucl.Phys.*, A651:289–319, 1999.

[35] N. B. Shul'gina, B. V. Danilin, V. D. Efros, J. M. Bang, J. S. Vaagen, and M. V. Zhukov. Three-body structure of $^8Li$ and the $^7\mathrm{Li}(n,\gamma)^8\mathrm{Li}$ reaction. *Nuclear Physics A*, 597(2):197 – 211, 1996.

[36] L.V. Grigorenko, B.V. Danilin, V.D. Efros, N.B. Shul'gina, and M.V. Zhukov. Extended three cluster model with two cluster long range correlations: Application to the $^8Li$ , $^8B$ nuclei. *Phys.Rev.*, C60:044312, 1999.

[37] P. Descouvemont and D. Baye. Microscopic study of the $^7Li(n,\gamma)^8Li$ and $^7Be(p,\gamma)^8B$ reactions in a multiconfiguration three-cluster model. *Nuclear Physics A*, 567(2):341 – 353, 1994.

[38] T.A. Tombrello. The capture of protons by $^7Be$. *Nucl. Phys.*, 71:459, 1965.

[39] J. T. Huang, C. A. Bertulani, and V. Guimaraes. Radiative capture of nucleons at astrophysical energies with single-particle states. *At. Data Nuc. Data Tables*, 96:824, 2010.

[40] The Facility for Rare Isotope Beams (FRIB) at the Michigan State University, http://frib.msu.edu/.

[41] G. Rupak and R. Higa. Model-Independent Calculation of Radiative Neutron Capture on Lithium-7. *Phys.Rev.Lett.*, 106:222501, 2011.

[42] S. Typel and G. Baur. Electromagnetic strength of neutron and proton single- particle halo nuclei. *Nucl. Phys.*, A759:247–308, 2005.

[43] L. Trache, A. Azhari, F. Carstoiu, H.L. Clark, C.A. Gagliardi, Y.W. Lui, A.M. Mukhamedzhanov, X. Tang, N. Timofeyuk, and R.E. Tribble. Asymptotic normalization coefficients for ${}^8B \rightarrow^7 Be + p$ from a study of ${}^8Li \rightarrow^7 Li + n$. *Phys.Rev.*, C67:062801, 2003.

[44] J. E. Lynn, E. T. Jurney, and S. Raman. Direct and valence neutron capture by $^7Li$. *Phys. Rev. C*, 44(2):764, 1991.

[45] L. Koester, K. Knopf, and W. Waschkowski. Neutron scattering length of lithium and boron and their isotopes. *Zeitschrift fr Physik A Atoms and Nuclei*, 312(1-2):81–88, 1983.

[46] C. Angulo, M. Azzouz, P. Descouvemont, G. Tabacaru, D. Baye, M. Cogneau, M. Couder, T. Davinson, A. Di Pietro, P. Figuera, M. Gaelens, P. Leleux, M. Loiselet, A. Ninane, F. de Oliveira Santos, R.G. Pizzone, G. Ryckewaert, N. deSrville, and F. Vanderbist. Experimental determination of the $^7Be+p$ scattering lengths. *Nuclear Physics A*, 716(0):211 – 229, 2003.

[47] S.Y. Choi, J. Lee, J. S. Shim, and H.S. Song. Spin-2 particle polarization. *J. Korean Phys. Soc.*, 25:576, 1992.

[48] S. Fleming, T. Mehen, and I. W. Stewart. NNLO corrections to nucleon nucleon scattering and perturbative pions. *Nucl. Phys.*, A677:313–366, 2000.

[49] N. J. Stone. Table of Nuclear Magnetic Dipole and Electric Quadruple Moments. *At. Data Nuc. Data Tables*, 96:75, 2005.

[50] D.B. Kaplan, M. J. Savage, and M. B. Wise. A new expansion for nucleon nucleon interactions. *Phys. Lett.*, B424:390–396, 1998.

[51] M. C. Birse, J. A. McGovern, and K. G. Richardson. A Renormalization group treatment of two-body scattering. *Phys. Lett.*, B464:169–176, 1999.

[52] J. Gegelia. EFT and N N scattering. *Phys.Lett.*, B429:227–231, 1998.

[53] U. van Kolck. Nucleon-nucleon interaction and isospin violation. 1997.

[54] U. van Kolck. Effective field theory of short range forces. *Nucl.Phys.*, A645:273–302, 1999.

[55] J.-W. Chen, G. Rupak, and M. J. Savage. Nucleon nucleon effective field theory without pions. *Nucl. Phys.*, A653:386–412, 1999.

[56] V. Pascalutsa and D.R. Phillips. Effective theory of the delta(1232) in Compton scattering off the nucleon. *Phys.Rev.*, C67:055202, 2003.

[57] F. C. Barker. The low-energy $^7\mathrm{Be}(p,\gamma)^8\mathrm{B}$ cross section from an r-matrix approach. *Nucl. Phys.*, A588:693, 1995.

[58] J. C. Blackmon, A. E. Champagne, J. K. Dickens, J. A. Harvey, M. A. Hofstee, S. Kopecky, D. C. Larson, D. C. Powell, S. Raman, and M. S. Smith. $^7Li(n,\gamma)^8Li$ cross sections at $E_n$=1.5–1340 ev. *Phys. Rev. C*, 54:383–388, 1996.

[59] J. J. Sakurai. *Modern Quantum Mechanics*. Addison Wesley Longman, New York, 1994.

[60] B. Long and U. van Kolck. pi N Scattering in the Delta(1232) Region in an Effective Field Theory. *Nucl.Phys.*, A840:39–75, 2010.

[61] H. W. Hammer and D. Lee. Causality and universality in low-energy quantum scattering. *Phys. Lett.*, B681:500–503, 2009.

[62] H. W. Hammer and D. Lee. Causality and the effective range expansion. *Annals Phys.*, 325:2212–2233, 2010.

[63] S Typel. Private communication.

[64] W. L. Imhof, R. G. Johnson, F. J. Vaughn, and M. Walt. Cross sections for the $^7Li(n,\ \gamma)^8Li$ reaction. *Phys. Rev.*, 114(4):1037–1039, 1959.

[65] Y. Nagai, M. Igashira, T. Takaoka, T. Kikuchi, T. Shima, A. Tomyo, A. Mengoni, and T. Otsuka. $^7Li(n,\gamma)^8Li$ reaction and the $S_{17}$ factor at $E_{c.m.} > 500$ keV. *Phys. Rev. C*, 71:055803, 2005.

[66] G. Rupak and N. Shoresh. NNLO Calculation of Two-Nucleon Scattering in EFT for a Two Yukawa Toy Model. *Phys. Rev.*, C60:054004, 1999.

[67] D. R. Phillips, G. Rupak, and M. J. Savage. Improving the convergence of N N effective field theory. *Phys. Lett.*, B473:209–218, 2000.

[68] T. D. Cohen, B. A. Gelman, and U. van Kolck. An Effective field theory for coupled channel scattering. *Phys.Lett.*, B588:57–66, 2004.

[69] M. Wiescher, J. Gorres, and F.-K. Thielemann. Capture reactions on C-14 in non-standard big bang nucleosynthesis. *Astrophys J.*, 363:340–343, 1990.

[70] T. Kajino, G. J. Mathews, and G. M. Fuller. Primordial nucleosynthesis of intermediate-mass elements in baryon-number-inhomogeneous big bang models - Observational tests. *Astrophys. J.*, 364:7–14, 1990.

[71] H. Beer, M. Wiescher, F. Kaeppeler, J. Goerres, and P.E. Koehler. A measurement of the C-14(n, gamma)C-15 cross section at a stellar temperature of kT = 23.3 keV. *Astrophys. J.*, 387:258, 1992.

[72] R. Reifarth, M. Heil, R. Plag, U. Besserer, S. Dababneh, L. Drr, J. Grres, R.C. Haight, F. Kppeler, A. Mengoni, S. O'Brien, N. Patronis, R.S. Rundberg, M. Wiescher, and J.B. Wilhelmy. Stellar neutron capture rates of $^{14}C$. *Nuclear Physics A*, 758(0):787 – 790, 2005.

[73] R. Reifarth, M. Heil, C. Forssén, U. Besserer, A. Couture, S. Dababneh, L. Dörr, J. Görres, R. C. Haight, F. Käppeler, A. Mengoni, S. O'Brien, N. Patronis, R. Plag, R. S. Rundberg, M. Wiescher, and J. B. Wilhelmy. The $^{14}C(n,\gamma)$ cross section between 10 kev and 1 Mev. *Phys. Rev. C*, 77:015804, 2008.

[74] A. Horvth , J. Weiner, A. Galonsky, F. Dek, Y. Higurashi, K. Ieki, Y. Iwata, . Kiss, J. J. Kolata, Z. Seres, J. von Schwarzenberg, H. Schelin, S. Takeuchi, S. Typel and R. E. Warner. Cross Section for the Astrophysical $^{14}C(n,\gamma)^{15}C$ Reaction via the Inverse Reaction. *Astrophys. J.*, 570:926, 2002.

[75] U. D. Pramanik, T. Aumann, K. Boretzky, B.V. Carlson, D. Cortina, T.W. Elze, H. Emling, H. Geissel, A. Grnschlo, M. Hellstrm, S. Ilievski, J.V. Kratz, R. Kulessa, Y. Leifels, A. Leistenschneider, E. Lubkiewicz, G. Mnzenberg, P. Reiter, H. Simon, K. Smmerer, E. Wajda, and W. Walus. Coulomb breakup of the neutron-rich isotopes $^{15}C$ and $^{17}C$ . *Physics Letters B*, 551(12):63 – 70, 2003.

[76] T. Nakamura, N. Fukuda, N. Aoi, H. Iwasaki, T. Kobayashi, T. Kubo, A. Mengoni, M. Notani, H. Otsu, H. Sakurai, S. Shimoura, T. Teranishi, Y. X. Watanabe, K. Yoneda, and M. Ishihara. Coulomb dissociation of halo nuclei. *Nucl. Phys. A*, 722:301, 2003.

[77] T. Nakamura, N. Fukuda, N. Aoi, N. Imai, M. Ishihara, H. Iwasaki, T. Kobayashi, T. Kubo, A. Mengoni, T. Motobayashi, M. Notani, H. Otsu, H. Sakurai, S. Shimoura, T. Teranishi, Y. X. Watanabe, and K. Yoneda. Neutron capture cross section of C14 of astrophysical interest studied by Coulomb breakup of C15. *Phys. Rev. C*, 79:035805, 2009.

[78] G. Baur, C.A. Bertulani, and H. Rebel. Coulomb dissociation as a source of information on radiative capture processes of astrophysical interest. *Nucl.Phys.*, A458:188–204, 1986.

[79] N. C. Summers and F. M. Nunes. Extracting $(n, \gamma)$ direct capture cross sections from coulomb dissociation: Application to $^{14}C(n, \gamma)^{15}C$. *Phys. Rev. C*, 78:011601, 2008.

[80] H. Esbensen. Coulomb dissociation of $^{15}$C and radiative neutron capture on $^{14}$C. *Phys. Rev. C*, 80:024608, Aug 2009.

[81] N. K. Timofeyuk, D. Baye, P. Descouvemont, R. Kamouni, and I. J. Thompson. $^{15}$C-$^{15}$F charge symmetry and the $^{14}\mathrm{C}(n, \gamma)^{15}\mathrm{C}$ reaction puzzle. *Phys. Rev. Lett.*, 96:162501, 2006.

[82] P. Descouvemont. Microscopic cluster study of the 15,17,19 C isotopes. *Nuclear Physics A*, 675(34):559 – 571, 2000.

[83] C. Wang, O. I. Cissé, and D. Baye. Parametrization of low-energy cross sections for nonresonant neutron capture. *Phys. Rev. C*, 80:034611, 2009.

[84] W. A. Fowler, G. R. Caughlan, and B. A. Zimmerman. Thermonuclear Reaction Rates. *Ann. Rev. Astr. Astrophys.*, 5:525, 1967.

[85] C.A. Bertulani. Theory and Applications of Coulomb Excitation. 2009.

[86] G. Rupak, L. Fernando, and A. Vaghani. Radiative neutron capture on carbon-14 in effective field theory. *Phys. Rev. C*, 86:044608, 2012.

[87] B. Acharya and D. R. Phillips. $^{19}C$ in halo EFT: Effective-range parameters from Coulomb dissociation experiments. *Nuclear Physics A*, 913(0):103 – 115, 2013.

[88] H. Kitagawa. Shell model calculation of magnetic moments of mirror nuclei (A = 8 - 13). *Progress of Theoretical Physics*, 102(2):273–285, 1999.

[89] K. Asahi, K. Sakai, H. Ogawa, H. Miyoshi, K. Yogo, A. Goto, T. Suga, H. Ueno, Y. Kobayashi, A. Yoshimi, A. Yoshida, T. Kubo, Y.X. Watanabe, H. Imai, K. Yoneda, N. Fukuda, N. Aoi, M. Ishihara, W.-D. Schmidt-Ott, G. Neyens, and S. Teughels. Electromagnetic moments of neutron-rich nuclei measured with polarized radioactive ion beams. *Nuclear Physics A*, 704(14):88 – 97, 2002.

[90] Nörtershäuser, W. and Tiedemann, D. and Žáková, M. and Andjelkovic, Z. and Blaum, K. and Bissell, M. L. and Cazan, R. and Drake, G. W. F. and Geppert, Ch. and Kowalska, M. and Krämer, J. and Krieger, A. and Neugart, R. and Sánchez, R. and Schmidt-Kaler, F. and Yan, Z.-C. and Yordanov, D. T. and Zimmermann, C. Nuclear Charge Radii of $^{7,9,10}$Be and the One-Neutron Halo Nucleus $^{11}$Be. *Phys. Rev. Lett.*, 102:062503, 2009.

[91] H.-W. Hammer and D.R. Phillips. Electric properties of the beryllium-11 system in halo EFT. *Nuclear Physics A*, 865(1):17 – 42, 2011.